Journal of
Materials Chemistry A

ROYAL SOCIETY
OF CHEMISTRY

REVIEW

View Article Online
View Journal | View Issue

Check for updates

Cite this: *J. Mater. Chem. A*, 2024, **12**, 29335

Advances in the application of first principles calculations to phosphate-based NASICON battery materials

Zhongyi Cui, Shilong Sun, Gexuan Ning, Lisi Liang, * Zeming Wang, Jiangyu Qiao, Lixing Zhang, Jin Chen and Zhuyue Zhang

Received 17th July 2024
Accepted 1st October 2024

DOI: 10.1039/d4ta04943h

rsc.li/materials-a

Sodium-ion batteries are a promising area of research, and phosphate-based sodium superionic conductor (NASICON) materials have received significant attention from researchers due to their high structural stability and ionic conductivity. First principles calculations have been employed to facilitate the research process. This paper introduces the application of first principles calculations in the study of battery materials. It reviews the research progress of the application of first principles calculations in phosphate-based NASICON structured cathode, anode and electrolyte materials, which mainly include the intrinsic properties of the materials and the study of ionic doping modification of some of the materials. It is demonstrated that NASICON materials exhibit excellent structural stability, an appropriate working voltage (approximately 2–4.2 V for cathode materials and below 2 V for anode materials) and an exceptional sodium ion transport performance (Na^+ migration barrier less than 1 eV), which collectively render them highly promising for application. However, the poor electronic conductivity (mostly semiconductor materials, with a band gap of 2–3 eV or so) limits the performance of the material. Ion doping can improve the electronic conductivity of the material to a certain extent, but the NASICON battery materials still cannot be compared with the current commercial lithium-ion battery materials. Consequently, multiple ion doping and conductive material modification will be some of the future research directions. As computers and computing software progress, first principles calculations could eventually become the standard approach for studying battery materials. This strategy might make it more straightforward to select the best battery materials and modification methods while including experimental testing to enhance the phosphate-based NASICON materials' overall performance and develop new battery materials.

1. Introduction

As a result of the worsening global energy crisis and environmental pollution, the development of new clean energy sources, such as solar energy and wind energy, which can be considered as alternatives to fossil fuels, has been greatly accelerated.[1–3] In addition, electrochemical energy storage devices, such as lithium-ion batteries, have been developed at a rapid pace and employed in a multitude of energy storage applications, including mobile phones, computers, electric vehicles, and grid energy storage.[4] Nevertheless, the high cost of raw materials has constrained the advancement of lithium-ion batteries. In contrast, the abundance of raw materials, low cost (relative to that of lithium-ion battery raw materials, which can be reduced by 50 times), and the similarity of mechanisms and greater potential for application make sodium-ion batteries a subject of interest to researchers.[5–9] The cathode materials currently employed in sodium-ion batteries include layered transition metal oxide cathode materials, Prussian blue analogues and polyanionic cathode materials.[10–12] As a representative example of a polyanion-type cathode material, sodium superionic conductor (NASICON) has been subjected to further investigation due to its high ionic conductivity and structural stability.[13,14] Furthermore, it can be employed as anode materials[15,16] and electrolyte materials[17–23] for sodium-ion batteries.

Sodium superionic conductor NASICON was first identified by Hong, Goodenough and Kafalas *et al.*[24,25] with the general formula $Na_xMM'(XO_4)_3$ (M/M′ = V, Fe, Nb, Ti… ; X = P, Si or S; $x = 0$ to 4). The crystal structure of $Na_xMM'(XO_4)_3$ with rhombohedral symmetry is depicted in Fig. 1, which comprises $[M(M')O_6]$ octahedra and $[XO_4]$ tetrahedra connected by the angular sharing of O to form the so-called $[MM'(XO_4)_3]^{3-}$ unit. The sodium ions occupy the interstices of the above units, dividing them into M[1] sites hexa-coordinated with O and M[2] sites octa-coordinated according to the filling positions. This unique three-dimensional spatial structure of the NASICON material has been demonstrated to exhibit higher ionic conductivity and

---

College of Metallurgical Engineering, Xi'an University of Architecture and Technology, Xi'an 710055, China. E-mail: 44406200@qq.com

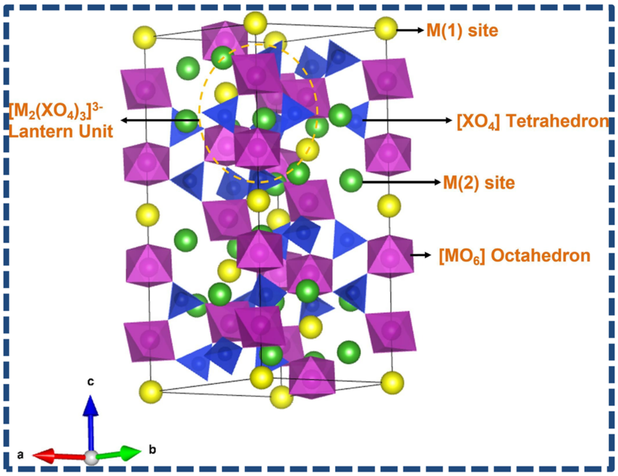

Fig. 1 The crystal structure of $Na_xMM'(XO_4)_3$ with rhombohedral symmetry. Reproduced from ref. 14 with permission from Elsevier, copyright 2023.

cycling stability than other sodium-ion battery materials in practice.[26] However, it should be noted that this structure also results in lower electronic conductivity, which in turn reduces the electrochemical performance of the material. Currently, researchers have employed a range of techniques to enhance the electronic conductivity and electrochemical properties of the materials, including ionic doping,[27,28] material nano-engineering,[29,30] and carbon-based material coating.[31,32] In addition to experimental methods, researchers frequently utilise first principles calculations to investigate various properties of materials.

First principles calculations based on density functional theory (DFT) employ a computer system to approximate the Schrödinger equation of complex systems, thereby enabling the acquisition of a wide range of chemical properties.[33] This approach eliminates the need for complex experimental processes and offers a high degree of accuracy. At present, the application of first principles calculations in batteries is primarily concerned with the prediction of formation energy, theoretical capacity, average (de)intercalation potential of sodium ions, electronic structure, migration barriers, and other types of chemical properties. These findings guide the research and development of new battery materials.[34,35] First principles calculation has also been employed in numerous applications during the research process of phosphate-based NASICON battery materials,[14,36] and this paper reviews the application of first principles calculations in NASICON battery materials and the current status of research in light of the existing literature, with a view to providing a reference for future research of NASICON materials.

2. First principles calculations of battery material properties

2.1 The formation energy

The formation energy can be employed to assess the phase stability of the battery material during the charging and discharging processes. For the sodium-ion battery electrode material $Na_{(z-x)}$host (where $z - y \leq x \leq 0$, z represents the maximum sodium embedded in the electrode material of the sodium-ion battery, x represents the amount of sodium removed, and $z - y$ represents the maximum amount of sodium removed; the formation energy, $E_f[Na_{(z-x)}host]$, with respect to the Na_zhost and the Na_yhost is obtained by using eqn (1):

$$E_f[Na_{z-x}host] = E[Na_{z-x}host] - \frac{x-y}{z-y}E[Na_z host] - \frac{z-x}{z-y}E[Na_y host] \qquad (1)$$

where $E[X]$ is the energy of X obtained from first principles calculation ($X = Na_{(z-x)}$host, Na_yhost, Na_zhost). By using $E[X]$ as the vertical coordinate and x as the horizontal coordinate, connecting $E[X]$, and ensuring that the resulting image is convex, one can obtain the formation energy convex hulls. This is accomplished by finding the equivalent formation energy E_f by varying the value of x ($0 < x \leq z$). The stable phase of the electrode material Na_zhost during the charging and discharging process is represented by the phase on the formation energy convex hulls.

2.2 Sodium average (de)intercalation potential and theoretical capacity

The operational mechanism of sodium-ion battery cathode materials is analogous to that of lithium-ion batteries, exhibiting reversible Na^+ detachment and embedding during the charging and discharging processes. As a result, first principles calculations that are comparable to the formula presented by Aydinol *et al.*[37] for determining the average (de)intercalation potential of lithium can be used to calculate the Na^+ (de)intercalation potential. Take the cathode materials for sodium-ion batteries as an example. When the reversible process (the forward reaction while charging and the reverse reaction during discharging) occurs, as indicated by eqn (2):

$$Na_z host - xNa^+ - xe^- \overset{\Delta G}{\leftrightarrow} Na_{z-x}host \qquad (2)$$

where z represents the maximum amount of sodium embedded in the Na_zhost, x represents the amount of sodium ions dislodged, and ΔG represents the amount of Gibbs free energy change at a temperature of 0 K, which is approximated by first-principles calculations. Based on the relationship between the amount of Gibbs free energy change of the reaction (ignoring the pV and entropy contributions during the reaction) and the electrode potential, the average sodium (de)intercalation potential of the anode material can be approximated as shown in eqn (3):

$$V = -\frac{\Delta G}{xF} = -\frac{E[Na_z host] - (E[Na_{z-x}host] + xE[A])}{xF} \qquad (3)$$

In this context, F represents the Faraday constant. Further generalisation allows us to derive the average sodium (de) intercalation potential between any two phases, the Na_{x_1}host and Na_{x_2}host (where $x_1 < x_2$), as illustrated in eqn (4).

$$V = -\frac{\Delta G}{(x_2 - x_1)F} = -\frac{E[Na_{x_2}host] - (E[Na_{x_1}host] + (x_2 - x_1)E[Na])}{(x_2 - x_1)F} \qquad (4)$$

By modifying the values of x_1 and x_2 and calculating the corresponding sodium release potentials, it is possible to obtain an average sodium release potential curve. This is achieved by taking the calculated average sodium (de)intercalation potential V as the vertical coordinate and the sodium content as the horizontal coordinate. The potential curve of the electrode material can be approximated according to the average sodium (de)intercalation potential curve.

The theoretical specific capacity of the sodium-ion battery electrode material can also be calculated as shown in eqn (5):

$$C = \frac{nF}{3.6M} = \frac{26800n}{M} \tag{5}$$

In this equation, the quantity n represents the extent of sodium deintercalation, whereas the variable M signifies the molar mass of the electrode material. Table 1 presents the theoretical and actual capacities of common sodium-ion battery cathode materials.

2.3 The energy band structure and density of states

The energy band structure of the sodium ion battery material can be derived from first principles calculations, and the electrical conductivity of the material can be visualised from the energy band structure diagram. The crossing of the top of the valence band with the Fermi energy level shows that the material is conductive and possesses high conductivity. When the top of the valence band is situated at the Fermi energy level, the material is classified as a semiconductor. The band gap, which is derived from the value of the gap between the top of the valence band and the bottom of the conduction band, can be seen to decrease as the conductivity is enhanced. Conversely, when the top of the valence band is positioned below the Fermi energy level, the material is identified as an insulator. Moreover, the material's density of states, comprising the total density of states and the partial density of states, can be derived from first principles calculations. The combined total and partial density of states allows for the analysis of the redox reaction occurring during the (de)intercalation of sodium from the battery material, thus facilitating the investigation of the reaction mechanism of the battery material itself.

Table 1 The theoretical and actual capacities of cathode materials for common sodium-ion batteries

Materials	Theoretical capacities (mA h g^{-1})	Actual capacities (mA h g^{-1})	Ref.
$NaMnO_2$	244	190	38
$Na_3V_2(PO_4)_3$	118(2*e*) 176(3*e*)	167	39
$Na_3V_2(PO_4)_2F_3$	128(2*e*) 192(3*e*)	127.7	40
$Na_3Fe_2(PO_4)_3$	115	82.1	41
$NaFePO_4$	154	140	42
$NaVPO_4F$	143	111	43
$Na_2Mn[Fe(CN)_6]$	171	96.2	44
$Na_2Co[Fe(CN)_6]$	170	94.3	45

2.4 Charge population

The charge of each atom in the reaction process can be analysed through first principles calculations, which can be divided into Bader charge calculation[46] and Mulliken charge calculation[47] according to the different calculation methods. The interaction between atoms can be obtained from the change of charge. For example, the change in atomic valency can be obtained by calculating the charge distribution of each atom before and after the (de)intercalation of the sodium-ion battery material. The electrochemical reaction mechanism of the material can be elucidated further through the alteration of atomic valency, which can provide a theoretical foundation for the investigation of battery materials.

2.5 Crystal dynamics

In addition to electronic conductivity, which is dependent on the band gap reaction, battery material conductivity is also a factor in determining battery performance. Ionic conductivity is another aspect that must be considered. In a sodium-ion battery, the primary conductivity is that of the sodium ions, as indicated by the sodium-ion migration barrier and sodium-ion migration coefficient. A prerequisite for establishing the sodium ion migration barrier and mobility coefficient is an understanding of the lattice dynamics of the material. This entails the study of ionic conduction paths and the vibrational behaviour of the lattice within the material. First-principles calculations offer a straightforward method for monitoring the internal lattice dynamics of a material. To illustrate, in the case of electrode materials, the diffusion paths are relatively straightforward and can therefore be calculated directly by first-principles calculations. The structures preceding and following sodium ion (de)intercalation are employed as reactants and products, respectively, while transition state searches are conducted using techniques such as the nudged elastic band (NEB) method or the climbing image nudged elastic band (CI-NEB). These procedures ultimately yield the sodium ion migration barrier. The sodium ion migration barrier is employed to quantify the ability of sodium ions to migrate and subsequently to characterise the conductivity of sodium ions in electrode materials. The path with the smallest sodium ion migration barrier represents the ionic conduction path of the material. Furthermore, the lattice vibration of the material can be obtained by combining with valence bond fabrication analysis.

The complex diffusion paths inherent to electrolyte materials present a significant challenge in calculating their sodium ion migration properties through transition state search methods. Consequently, the prevailing approach for evaluating the overall migration properties of materials is through *ab initio* molecular dynamics (AIMD) based on statistical methods. The AIMD method can be employed to calculate the diffusion coefficient and the diffusion activation energy of a material through the Einstein–Smoluchowski relation and the Nernst–Einstein relation,[48] thereby enabling a quantitative characterisation of the sodium ion conductivity.[49] Furthermore, AIMD enables more accurate observation of the lattice dynamics of materials. For example, Yang *et al.*[50] employed first-principles molecular dynamics simulations to observe NASICON materials that facilitate ion migration through polyanion rotation. This approach resulted in the identification of three novel materials ($NaGaBr_4$, $NaNbCl_6$, and Na_4SiSe_4) exhibiting polyanion rotation behaviour. Meanwhile, the sodium ion migration performance and polyanion rotation of materials exhibiting polyanion rotation at high temperatures can be enhanced by the introduction of Na vacancies at low temperatures. This provides a framework for the design and development of new polyanion-rotating fast ion conductors.

3. Application of first principles calculations to NASICON

3.1 NASICON cathode materials

3.1.1 $Na_3V_2(PO_4)_3$. As a representative NASICION cathode material, $Na_3V_2(PO_4)_3$ is particularly well-suited for use as a cathode material in sodium-ion batteries, due to its exceptional thermal stability[51] and high multiplicity performance,[52,53] which are a result of its stable polyanionic structure,[54] high theoretical specific capacity (117.6 mA h g^{-1}), and high operating voltage (up to 3.4 V).[55] Since its discovery by J. Gopalakrishnan *et al.*[56] in 1992, the material has attracted the attention of many researchers. However, the poor electronic conductivity limits its performance. Carbon cladding,[57–59] carbon-based composites,[60,61] nanoengineering[62,63] and ion doping[64,65] have been utilised to enhance the electrochemical properties of the materials. Additionally, first-principles calculations have been integrated into the research process of $Na_3V_2(PO_4)_3$.

The intrinsic properties of $Na_3V_2(PO_4)_3$ (NVP) have been investigated through the application of first-principles methods. As stated by Gopalakrishnan *et al.*,[56] the atomic coordinates of NVP are presented in Table 2, which belong to the typical NASICON structure with space group $R3c$, exhibiting both Na[1] and Na[2] sites (both with an ionic occupancy of 0.75). These coordinates were employed in the first-principles calculations that were conducted to derive the exact configuration of NVP. Lim *et al.*[51] calculated the (de)intercalation potentials of NVP using first principles calculations. Their findings revealed that the stable phases of Na_xVP ($x = 0–4$) encompass Na_0VP, Na_1VP, Na_3VP and Na_4VP. Additionally, they observed that the sodium deintercalation process comprises $Na_1VP \rightarrow Na_0VP$ (average potential of 4.64 V), $Na_3VP \rightarrow Na_1VP$ (average potential of 3.40 V) and $Na_4VP \rightarrow Na_3VP$ (average potential of 2.03 V). Furthermore, first-principles calculations have been employed for the kinetic calculations of NVP. Wang *et al.*[67] conducted a first-principles calculation of the migration kinetics of NVP. Two potential migration pathways (Fig. 2(a)), denoted as path 1 (Na[2]–Na[2]) and path 2 (Na[1]–Na[2]), were considered. The calculated path 1 potential barrier was found to be lower at 0.292 eV (Fig. 2(b)), indicating that the sodium ion migration in NVP is more inclined to occur from Na[2]–Na[2]. This finding is corroborated by experimental studies.

In addition, first principles calculations have been applied in the ion doping studies of NVP, with the doping sites investigated encompassing Na-site doping, V-site doping and P-site doping. At present, the most extensively studied by using first-principles calculations is mainly V-site doping, with doping of

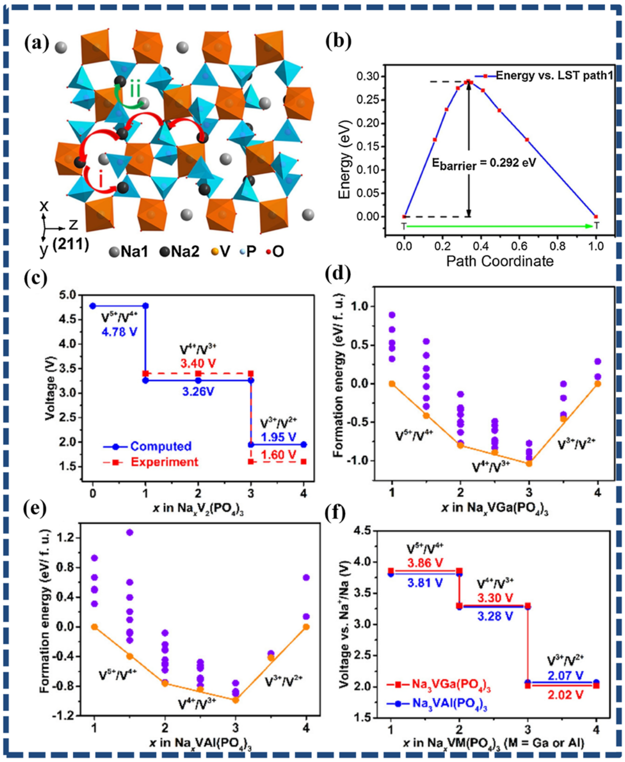

Fig. 2 (a) Na migration path in the lattice of $Na_3V_2(PO_4)_3$ bulk. (b) Energy curve along the Na diffusion path *i*. $E_{barrier}$ indicates the activation barrier of this process. Reproduced from ref. 67 with permission from Elsevier, copyright 2015. (c) Calculated voltage plateaus of $Na_3V_2(PO_4)_3$. The convex hull of (d) $Na_xVGa(PO_4)_3$ and (e) $Na_xVAl(PO_4)_3$ from DFT calculations. (f) Calculated voltage plateaus of $Na_3VM(PO_4)_3$ (M = Ga or Al). Reproduced from ref. 68 with permission from the American Chemical Society, copyright 2021.

Table 2 Atomic coordinates of $Na_3V_2(PO_4)_3$. Reproduced from ref. 66 with permission from Elsevier, copyright 2014

Site	Element	Wyckoff symbol	*x*	*y*	*z*	Occupation
O1	O	36*f*	0.01714	0.20172	0.19119	1
O2	O	36*f*	0.18532	0.16658	0.08488	1
P1	P	18*e*	0.29683	0	1/4	1
Na[1]	Na	18*e*	0.63747	0	1/4	0.75
V1	V	12*c*	0	0	0.14679	1
Na[2]	Na	6*b*	0	0	0	0.75

elements including Al, Ga, Ti, Mg, Mn, Cu, Fe, Zn, Nb, Co, Mo and so on. The effects are mainly reflected in the material bandgap, the (de)intercalation potentials and ion migration barriers. The material band gap is primarily altered through elemental doping, which modifies the material's electronic density of states. This approach reduces the band gap of the material by changing the density of states distribution of the material to lower the bottom position of the conduction band or increase the top position of the valence band. As illustrated in Table 4, doping at the V-site with Al, Ti, Zn, Nb, and Co has the effect of reducing the band gap of NVP.

Zhao *et al.*[69] employed a combination of first-principles calculations and experimental techniques to examine the impact of V-site Al doping on the properties of NVP. Their findings indicated that the electron affinity energies of the Al atoms are comparatively lower than those of the V atoms (0.441 and 0.525 eV for Al and V, respectively), resulting in a reduction in the band gap value of NVP. The electron affinity energy of Al atoms (0.525 eV) enables them to act as a donor dopant, thereby increasing the electronic conductivity.

This results in the conversion of the NVP bandgap from an indirect bandgap of 1.735 eV to a direct bandgap of 1.58 eV. Huang *et al.*[70] investigated the effect of Ti atom doping on NVP, as illustrated in Fig. 3(a) and (b). Density of states calculations demonstrated that Ti atom doping did not alter the density of states distribution of NVP, wherein the top of the valence band is occupied by the O 2p state and the bottom of the conduction band is occupied by the V 3d state. The sole consequence of this was a reduction in the material band gap, from 1.51 eV to 0.56 eV, as a result of the shift in the position of the conduction band bottom. Furthermore, Nb doping of the V-site of the NVP resulted in a reduction of the material band gap value from 1.51 eV to 0.76 eV,[71] while Co doping led to a decrease from 3.01 eV to 1.41 eV.[72]

Furthermore, elemental doping results in a modification of the sodium (de)intercalation potential of the material. Based on eqn (4), the sodium (de)intercalation potential of the material at 0 K can be calculated by first principles calculation. Wang *et al.*[68] employed first principles calculation to investigate the activation of the $V^{4+/5+}$ redox pair by V-site Al- or Ga-doped NVP, as illustrated in Fig. 2(c), the (de)intercalation of NVP from Na_3VP to Na_1VP. This process is accompanied by a $V^{3+/4+}$ redox reaction, while a $V^{4+/5+}$ reaction is not possible due to the excessively high potential (4.78 V) compared to the decomposition potential of the electrolyte. Fig. 2(d) and (e) present the formation energy convex hulls of NVMP (M = Ga/Al), which demonstrate that the reaction process of $V^{3+/4+}$ occurs in two phases between Na_2VMP and Na_3VMP. Through further calculations of the deintercalation potential curves (Fig. 2(f)), it was demonstrated that Ga/Al doping reduces the potential of the $V^{4+/5+}$ redox reaction and activates the $V^{4+/5+}$ redox pairs, thereby increasing the operating voltage of the material. Chen *et al.*[73] employed a combination of first-principles calculations and experiments to investigate the impact of Ga doping at the V-site on its properties and observed that the introduction of Ga^{3+} doping resulted in an increase in the electron density of V, the activation of the V^{4+}/V^{5+} redox pair, and a notable enhancement in the operating voltage (the emergence of a new 4 V voltage plateau) and the cycling stability of the material (an improvement in capacity retention from 67% to 90% after 70 cycles at 1C).

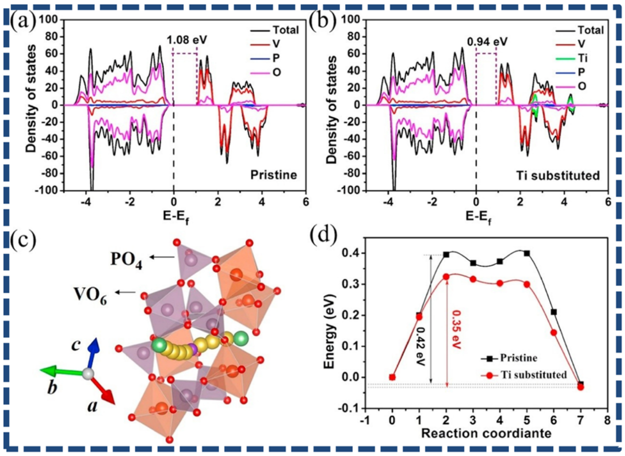

Fig. 3 The density of states: (a) NVP; (b) Ti-substituted NVP. (c) The calculated diffusion trajectory of Na ions along the intra-layer pathway in NVP and (d) the corresponding migration activation energy in NVP and Ti-substituted NVP. Reproduced from ref. 70 with permission from Elsevier, copyright 2018.

The charging and discharging of sodium-ion batteries is dependent upon the migration of sodium ions between the positive (negative) electrode and the electrolyte. Consequently, the sodium ion migration performance is a determining factor in the charging and discharging performance of the material. In the case of NVP materials, the migration of sodium ions is primarily facilitated through the gap between $[PO_4]$ tetrahedra and $[VO_6]$ octahedra. Li *et al.*[74] conducted an investigation into the sodium ion migration kinetics of NVPs, demonstrating that the migration of sodium ions occurs through intra-layer Na[1]–Na[2], Na[2]–Na[1] migration, or inter-layer Na migration. The calculations of ion mobility barriers indicate that the intra-layer mobility barrier is lower than the inter-layer one, with the intra-layer Na[1]–Na[2] and Na[2]–Na[1] mobility barriers being similar. Consequently, the NVP materials are primarily charged and discharged due to the intra-layer Na mobility. The doping of the V-site elements can alter the distance and Coulomb force between sodium ions in the same layer, as well as the diffusion channel of the sodium ions. This can reduce the ion mobility barriers to a certain extent, thereby enhancing the ionic conductivity.

Huang *et al.*[70] demonstrated that V-site Ti doping can reduce the distance between Na[2]–Na[1] and extend the sodium ion migration channel (Fig. 3(c)). As illustrated in Fig. 3(d), the sodium ion mobility barrier was reduced from 0.42 eV to 0.35 eV. Tong *et al.*[75] showed that the sodium ion mobility barrier was reduced from 0.457 eV to 0.402 eV by V-site Zn substitution. The enhancement of ionic conductivity is associated with the open sodium channel and the Coulomb force between sodium ions. Furthermore, V-site Mn,[76] Nb,[71] Co,[72] and Mo[74] substitution diminishes the sodium ion mobility barrier, as illustrated in Table 4. However, V-site doping does not invariably reduce the sodium ion mobility barrier, as evidenced by the findings of Zhao *et al.*[69] V-site Al doping has been observed to increase the sodium ion migration barrier (0.477 eV to 0.547 eV), which may be related to the atomic radius of the dopant atom X and the gap between the octahedra of dopant atoms [XO_6] and [PO_4]. This has the effect of reducing Na^+ migration.

The Na-site doping elements are predominately Li and K atoms that belong to the same family as Na. Their primary function is to enhance the electronic conductivity of NVP materials. In the investigation of Na-site Li doping, Zheng *et al.*[77] employed a combination of experimental and first-principles computational techniques to examine the impact of Li doping on NVP. Their findings revealed that Li doping tends to occupy the Na[3] site when the doping level is low, and shifts to the Na[1] and Na[2] sites when the doping level is high. Cong *et al.*[78] investigated the impact of Na-site Li doping on the performance of NVPs and discovered that Li doping was capable of enhancing its electrochemical performance, with the specific capacity increasing from 105 mA h g^{-1} to 116.9 mA h g^{-1} (close to the theoretical specific capacity of 117 mA h g^{-1}) at 0.2C. As illustrated in Fig. 4(a)–(f), the doping of Li was observed to activate Na^+ activity and reduce the band gap, thereby facilitating Na^+ migration, as determined by first-principles calculations. Additionally, investigated Na-site K doping was investigated,[79] as depicted in Fig. 4(g)–(l). It was observed that varying Na-site K doping can enhance the electronic conductivity of the material to a certain extent. Notably, Na[1]-site K doping exhibited the smallest bandgap and the optimal electronic conductivity. P-site doping represents a distinct form of doping, as elucidated by Hu *et al.*[80] who examined the impact of P-site B doping on the structure and electrochemical properties of the material. Their findings revealed that while B doping did not alter the material's structure, analysis of the density of states indicated that B doping resulted in a reduction of the bandgap. However, further increases in the amount of B doping did not result in a significant decrease in the bandgap. Furthermore, the doping of the material with a B atom in the conduction band at the bottom of the new V atomic energy state, resulting from the substitution of P^{5+} by B^{3+}, produces two holes that transfer to the two adjacent V atoms, thereby inducing the creation of a new energy level. Wang *et al.*[81] conducted further investigations into the impact of P-site B doping on the structure and electrochemical properties of the material, and DFT calculations demonstrated that B doping enhances the structural stability of the material and elevates the working voltage of the material. This is attributed to the more positive potential of the surrounding V atoms resulting from B doping, as well as a reduction in the lattice size to a certain extent and an increase in the Na^+ diffusion barrier.

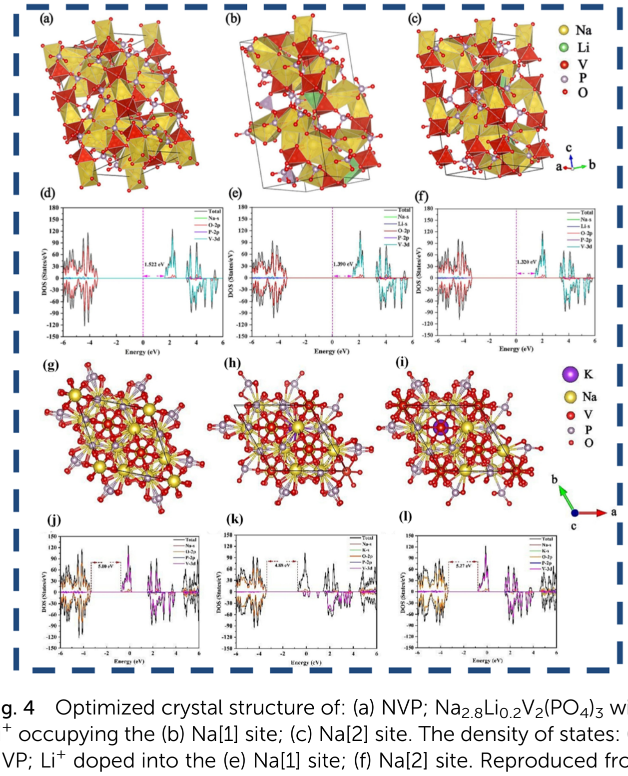

Fig. 4 Optimized crystal structure of: (a) NVP; $Na_{2.8}Li_{0.2}V_2(PO_4)_3$ with Li^+ occupying the (b) Na[1] site; (c) Na[2] site. The density of states: (d) NVP; Li^+ doped into the (e) Na[1] site; (f) Na[2] site. Reproduced from ref. 78 with permission from Elsevier, copyright 2024. Optimized crystal structure of (g) $Na_3V_2(PO_4)_3$ and (h) $Na_{2.9}K_{0.1}V_2(PO_4)_3$ with K^+ occupying the Na[1] site, (i) $Na_{2.9}K_{0.1}V_2(PO_4)_3$ with K^+ occupying the Na [2] site. The density of states: (j) $Na_3V_2(PO_4)_3$, with (k) K^+ occupying the Na[1] site and (l) K^+ occupying the Na[2] site. Reproduced from ref. 79 with permission from Elsevier, copyright 2023.

3.1.2 $Na_3V_2(PO_4)_2F_3$. The synthesis of $Na_3V_2(PO_4)_2F_3$ (NVPF) was initially reported by Le *et al.*[82] *via* a hydrothermal approach. Subsequent experimental characterisation revealed that the material exhibits a room temperature subordinate *P*4$_2$/*mnm* space group, with the atomic coordinates presented in Table 3. The specific structure of NVPF is illustrated in Fig. 5(a) and (b). In contrast to NVP, NVPF employs three F-atoms in place of one [PO_4] group. The [PO_4] tetrahedron and [$V_2O_8F_3$] octahedron form the [$V_2(PO_4)_2F_3$]$^{3-}$structure through corner sharing. The gap in the [$V_2(PO_4)_2F_3$]$^{3-}$ structure provides two storage sites for Na^+, denoted as Na[1] and Na[2]. Furthermore, the interatomic coulombic forces also lead to a different proportion of Na atoms occupying the two sites. Shakoor *et al.*[83] demonstrated that the Na atoms are fully occupied in the Na[1] site and half occupied in the Na[2] site. Additionally, the incorporation of F atoms enhances the material's operational potential, reaching 3.75 V. Song *et al.*[66] demonstrated through DFT calculations that the elevated operational potential of NVPF is attributed to the robust ionic V–F bond in NVPF, which provides augmented energy for the redox pairs of transition metals, thereby boosting the material's operational voltage and enhancing its electrochemical characteristics (the theoretical specific capacity ranges from 117 mA h g^{-1} in NVP to 128 mA h g^{-1} in NVPF). The enhanced working potential, specific capacity and stable structure render the NVPF material an optimal cathode for sodium-ion batteries. Moreover, first-principles calculations have been employed in the property calculations and ion doping studies of NVPF.

In a pioneering study, Shakoor *et al.*[83] explored the potential of NVPF in sodium-ion secondary batteries, integrating first-principles calculations and experimental techniques. A comparison of the structural optimisation results of the first-principles calculations with the structural parameters obtained

Table 3 Atomic coordinates of $Na_3V_2(PO_4)_2F_3$. Reproduced from ref. 66 with permission from Elsevier, copyright 2014

Site	Element	Wyckoff symbol	*x*	*y*	*z*	Occupation
Na[1]	Na	8*i*	0.5234(3)	0.2299(5)		1
Na[2]	Na	8*i*	0.803(1)	0.0512(8)		0.5
V	V	8*j*	0.24783(6)	0.24783(6)	0.18845(4)	1
P1	P	4*d*				1
P2	P	4*e*			0.2553(1)	1
O1	O	16*k*	0.0969(4)	0.4059(4)	0.1629(5)	1
O2	O	8*j*	0.0947(4)	0.0947(4)	0.1682(5)	1
O3	O	8*j*	0.4031(4)	0.4031(4)	0.1605(5)	1
F1	F	4*f*	0.2476(3)	0.2476(3)		1
F2	F	8*j*	0.2466(2)	0.2466(2)	0.3642(2)	1

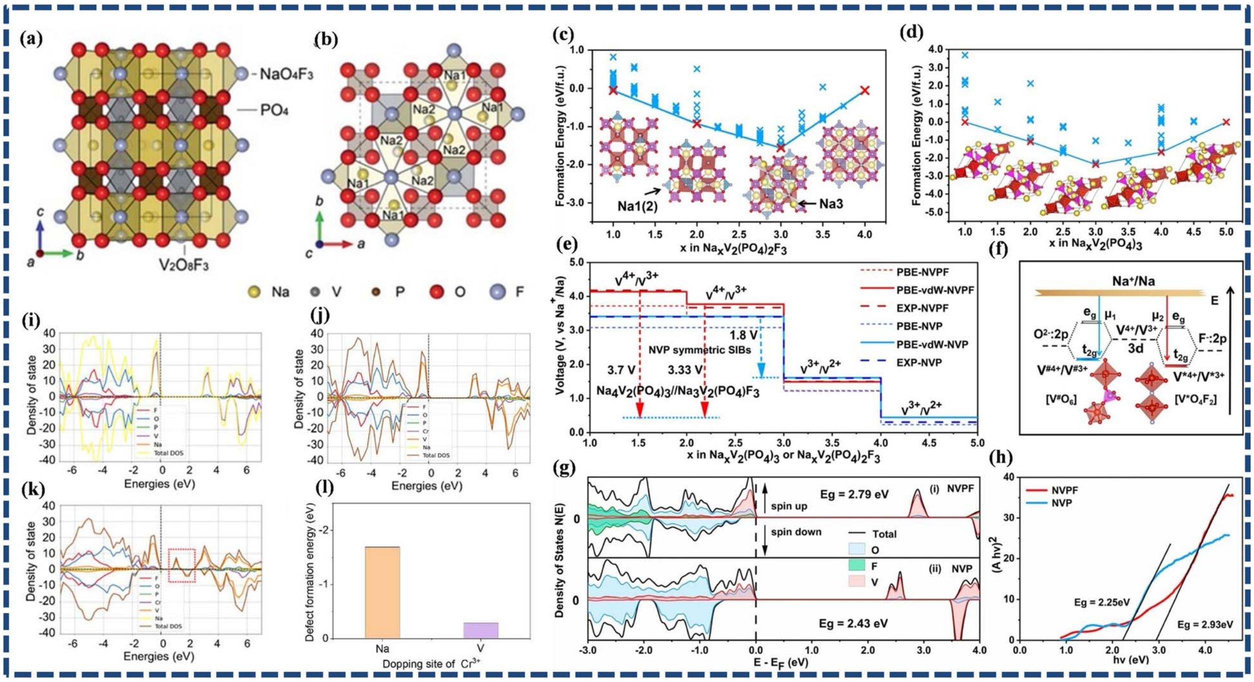

Fig. 5 Schematic representation of a refined $Na_3V_2(PO_4)_2F_3$ structure projected along (a) the *a* axis and (b) the *c* axis. Reproduced from ref. 83 with permission from the Royal Society of Chemistry, copyright 2012. Convex hulls and the simulated sodiation/desodiation behaviors of (c) $Na_xV_2(PO_4)_2F_3$ and (d) $Na_xV_2(PO_4)_3$. (e) The calculated and experimental voltage plateaus of $Na_xV_2(PO_4)_3$ and $Na_xV_2(PO_4)_2F_3$. (f) Molecular orbital energy diagram of the $[VO_6]$ octahedron and $[VO_4F_2]$ octahedron. (g) The density of states (DOS) of (i) $Na_3V_2(PO_4)_2F_3$ and (ii) $Na_3V_2(PO_4)_3$. (h) The calculated band gaps of $Na_3V_2(PO_4)_2F_3$ and $Na_3V_2(PO_4)_3$ from UV-vis absorption spectra. Reproduced from ref. 84 with permission from Elsevier, copyright 2023. DFT calculations: calculated density of states (DOS) for (i) $Na_{12}V_8P_8O_{32}F_{12}$, (j) $Na_{12}V_7CrP_8O_{32}F_{12}$, and (k) $Na_9CrV_8P_8O_{32}F_{12}$ using the HSE functional; (l) defect formation energy for Cr^{3+} doping in Na or V sites. Reproduced from ref. 85 with permission from Elsevier, copyright 2023.

from XRD and ND characterisation revealed the presence of fully occupied and half-occupied sites in NVPF, as illustrated in Fig. 5(b). Additionally, first principles calculations indicated that NVPF exhibits a sodium deintercalation potential as high as 3.81 V. Following the integration of experimental electrochemical tests, it was ultimately determined that NVPF can be employed as an efficient cathode material for sodium-ion batteries, as opposed to lithium-ion batteries, following a period of continuous optimisation. This conclusion was also corroborated by the findings of Geng *et al.*[86]

Lin *et al.*[84] designed a class of quasi-symmetric sodium-ion batteries ($Na_4V_2(PO_4)_3//Na_3V_2(PO_4)_2F_3$ Q-SSIB) using first-principles calculations. First, the formation energy convex hulls of NVP and NVPF were calculated. It was found that the stable phases of $Na_xV_2(PO_4)_3$ are at $x = 1, 2, 3, 4, 5$, whereas the stable phases of $Na_xV_2(PO_4)_2F_3$ are at $x = 1, 2, 3, 4$, as shown in Fig. 5(c) and (d). Subsequently, the sodium deintercalation potential maps of the two cell materials were obtained (Fig. 5(e)). By comparing the potentials calculated by different methods with the experiments, it was found that the difference in the potential of the $Na_4V_2(PO_4)_3//Na_3V_2(PO_4)_2F_3$ cell obtained by PBE-vdW (3.7 V) is much closer to the experimental result (3.75 V). This demonstrates the feasibility of the two materials as a full sodium-ion battery. Furthermore, the author examined the reason behind the higher operating potential of NVPF in comparison to NVP. As illustrated in Fig. 5(f), the higher electronegativity of F atoms in comparison to O atoms results in a lower redox energy of $V^{3+/4+}$ in NVPF (relative to Na^+ Fermi energy), which consequently leads to an increase in the operating potential. The density of states of NVP and NVPF were calculated by DFT as shown in Fig. 5(g). The density of states of F atoms in NVPF is predominantly situated below −2 eV in comparison to NVP, which is considerably lower than that of O atoms. The combination of the electron localisation function (ELF) diagrams demonstrates that the F atoms are more localised than the O atoms, which corroborates the aforementioned analysis. Furthermore, the incorporation of F atoms results in an augmentation of the band gap value (up to 2.79 eV) and a reduction in electronic conductivity (as illustrated in Fig. 5(h)). The results of experimental electrochemical tests demonstrate that the $Na_4V_2(PO_4)_3//Na_3V_2(PO_4)_2F_3$ Q-SSIB full cell is capable of discharging a high energy density of 340 W h kg^{-1} at 1C, as well as maintaining an operating voltage of up to 3.75 V.

However, the poor electronic conductivity of NVPF limits its performance. To enhance the electronic conductivity of the material, carbon-based material coating, material nanostructure design and ion doping are primarily employed. First-principles calculations have been utilised in studies of ion doping modifications to NVPF, with the majority of doping occurring at the Na and V sites. In a study by Zhang *et al.*,[87] the density of states and sodium ion migration barriers of K-doped NVPF and pure NVPF materials were compared using first-principles calculations. K-doped NVPF exhibited a lowered bandgap (from 2.75 eV to 2.68 eV) and sodium ion migration barrier (from 187 meV to 128 meV), which enhanced the conductivity of the material. The enhanced conductivity resulted in an improvement in the electrochemical performance and cycle life of the material. Specifically, the specific capacity of the material discharge increased from 110.6 mA h g^{-1} to 120.7 mA h g^{-1} at 0.1C, while the capacity retention after 500 cycles increased from 78 to 97.5%. Yi *et al.*[85] employed Cr^{3+} for NVPF doping modification and conducted a comparative analysis of the density of states of V-site doped Cr^{3+}, Na-site doped Cr^{3+} and pure NVPF using DFT calculations (Fig. 5(i)–(k)). It was discovered that Na-site doping of Cr^{3+} results in the generation of new energy levels at the bottom of the conduction band, which significantly reduces the band gap value of the material (from 3.29 eV to 1.35 eV) and enhances the intrinsic electronic conductivity of the material. Furthermore, the defect formation energy calculations (Fig. 5(l)) indicate that the defect formation energy of Na-site doped Cr^{3+} is lower, thereby suggesting that Cr^{3+} exhibits a preference for Na-site doping. In comparison to K doping, Cr doping substantially enhances the electrochemical performance of NVPF. Specifically, the specific capacity of discharge at 1C increased from 104.2 mA h g^{-1} to 117.7 mA h g^{-1}. This improvement may be attributed to the fact that Cr doping significantly elevates the electronic conductivity of NVPF.

The V-site doping elements calculated by DFT include Ti,[88] Fe,[89] W,[90] Al,[91] and others. However, due to the disparate approximation methods, cut-off energies, and convergence criteria employed in the calculations, it is not feasible to directly compare the band gap values to demonstrate the enhancement of the electronic conductivity of the material. Nevertheless, the incorporation of these dopant elements has resulted in a reduction in the band gap value of NVPF. Yi *et al.*[88] investigated the impact of distinct valence state Ti^{x+} (Ti^{2+}, Ti^{3+}, and Ti^{4+}) doping on the performance of NVPF materials. It was demonstrated that the substitution of Ti^{2+} for V^{3+} can markedly enhance the electrochemical performance of the material, as evidenced by an increase in the specific capacity at 0.2C from 105 mA h g^{-1} to 125 mA h g^{-1}, and a corresponding improvement in rate performance at 40C, with an increase in the specific capacity from 60 mA h g^{-1} to 104 mA h g^{-1}. DFT calculations indicate that the doping of Ti atoms results in a reduction of the band gap from 1.167 eV to 1.049 eV.

Li *et al.*[89] observed that the doping of Fe induces the migration of electrons near the V ion to Fe, which results in a gradual transformation of V^{3+} into V^{4+}. The valence state of Fe is lower than +3, enabling its participation in the redox reaction as an electron contributor during the charge and discharge process of NVPF. Additionally, the doping of Fe enhances the conductivity of the material, reducing the band gap of the material from 4.47 eV to 3.79 eV. Nongkynrih *et al.*[90] modified NVPF through the introduction of W doping. DFT calculations revealed that the substitution of V-site W^{6+} can facilitate the migration of a significant number of electrons to the conduction band, thereby reducing the band gap to 1.35 eV. Furthermore, the doping of Al atoms results in a change in the band gap, from 1.951 eV to 1.862 eV. Furthermore, the NVPF material requires a higher voltage (approximately 4.9 V *vs.* Na/Na^+) to facilitate the release of the third Na^+, which constrains its capacity. In a related study, Lubbe *et al.*[92] investigated the potential of transition metal doping to overcome the theoretical capacity limit of NVPF. A DFT calculation was conducted to assess the feasibility of replacing part of the V atoms in NVPF with Mo, Nb, and W. The phase stability and sodium deintercalation potential of these substitutions were evaluated. As illustrated in Fig. 6, the substitution of Mo for 50% of the V atoms in NVPF was observed to reduce the third Na^+ extraction potential by 0.6 V, thereby increasing the theoretical specific capacity of NVPF from 128 mA h g^{-1} to 174 mA h g^{-1}. However, the doping of Nb and W atoms resulted in a reduction of the potential to an extent that is not conducive to the enhancement of the energy density of the material. Additionally, the material migration barrier calculation indicates that Mo doping enhances the ionic conductivity of the material. Ultimately, it can be concluded that the doping of Mo atoms enhances the conductivity of the material and elevates its mass-specific energy density by 13.9% (from approximately 507 W h kg^{-1} to approximately 577.3 W h kg^{-1}).

3.1.3 Manganese phosphate-based NASICON cathode materials. Manganese phosphate-based NASICON materials represent another significant category of cathode materials, including $Na_4MnV(PO_4)_3$,[93,94] $Na_3MnZr(PO_4)_3$,[95] and $Na_3MnTi(PO_4)_3$ (ref. 96) materials that are capable of achieving energy storage through the electrochemical redox reaction

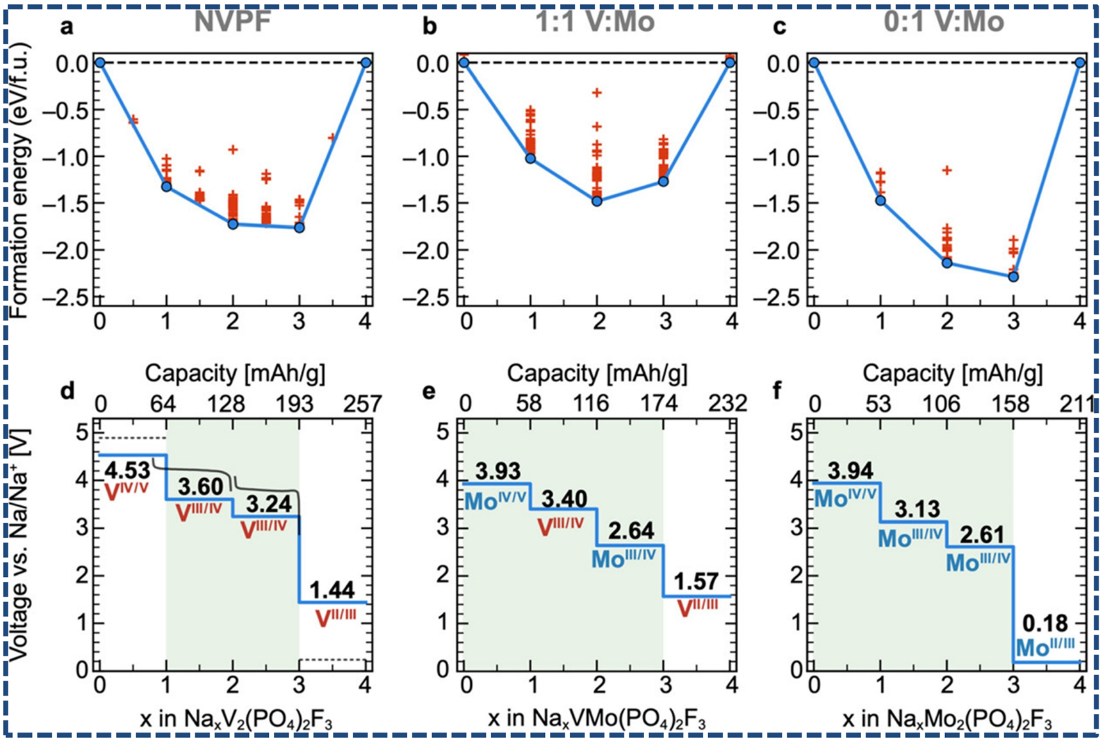

Fig. 6 anels a to c show the computed mixing energies (approximated by using formation energy) with GGA+U as a function of Na concentration x for N_xVPF (a), N_xVMoPF (b), and N_xMoPF (c). Unstable Na-vacancy orderings are shown by the red crosses, whereas ground state orderings (blue dots) form the phase diagram at 0 K—the convex hull. Panels d to f depict the corresponding intercalation voltages *vs.* Na/Na^+ as a function of Na concentration x for N_xVPF (d), N_xVMoPF (e), and N_xMoPF (f). Reproduced from ref. 92 with permission from the American Chemical Society, copyright 2023.

between $Mn^{2+}/Mn^{3+}/Mn^{4+}$. However, the two-electron reversible reaction and severe voltage hysteresis phenomenon also impose limitations on the performance of these materials, including the specific capacity. Consequently, first-principles calculations have been employed in the optimisation study of the performance of manganese phosphate-based NASICON materials.

For example, Wang *et al.*[97] investigated the $Na_4MnCr(PO_4)_3$ (NMCP) material. First-principles calculations revealed that the Mn/Cr-based materials have relatively low energies (<25 meV per atom) over the entire Na[1]–Na[4] region, indicating that these materials are accessible for synthesis and that the structure is stable upon (de)intercalation. Furthermore, the deintercalation potential calculations indicate that the combination of $Mn^{2+/3+}$, $Mn^{3+/4+}$ and $Cr^{3+/4+}$ redox pairs in NMCP provides an average voltage close to 4 V and a theoretical capacity of 165 mA h g^{-1}. Additionally, the calculations of lattice constant changes during denaturation suggest that the rate of change of the lattice parameter of the material during the denaturation of the third Na^+ is still relatively small (where $|\Delta a/a| = 1.18\%$, $|\Delta c/c| = 1.8\%$). This result corroborates the viability of the material for high sodium deintercalation. A combination of experimental synthesis and performance tests demonstrates that the NMCP material exhibits an average operating voltage of up to 3.59 V and a high reversible capacity of 130 mA h g^{-1}. However, the poor structural stability limits the further application of the material. Therefore, Li *et al.*98 mitigated the Jahn–Teller perturbation and improved the cycling life of the material by replacing Mn by Mg in a small amount. The results of DFT calculations and models are shown in Fig. 7. The introduction of Mg doping resulted in a reduction in the bandgap of the NMCP material (from 3.065 eV to 2.877 eV), accompanied by an increase in its highest migration barrier (0.51 eV), which is lower than that observed in other reported NASICON cathode materials.[99,100] The favourable electrical conductivity also results in favourable reaction kinetics and high multiplicity performance (154.6 and 70.4 mA h g^{-1} at 0.1 and 15C) of the $Na_4Mn_{0.9}CrMg_{0.1}(PO_4)_3$ material.

Liu *et al.*[101] conducted an investigation into the failure mechanism of $Na_3MnTi(PO_4)_3$, with the objective of optimising the material properties through the introduction of Mo doping. The results demonstrated that the failure of manganese phosphate-based materials was associated with the presence of internal antisite defects (IASD) during the synthesis process. AIMD calculations indicated that Mo doping could potentially enhance the Na^+ diffusion performance of the materials by reducing the concentration of defects. The experimental tests demonstrated that Mo doping resulted in an increase in the initial coulombic efficiency of the NMTP material from 76.2% to 85.9%, an increase in the initial capacity from 82.1 mA h g^{-1} to 103.7 mA h g^{-1} at 0.1C, and a retention of 78.7% of the initial capacity after 600 cycles at 0.5C in the voltage range of 2.5–4.2 V.

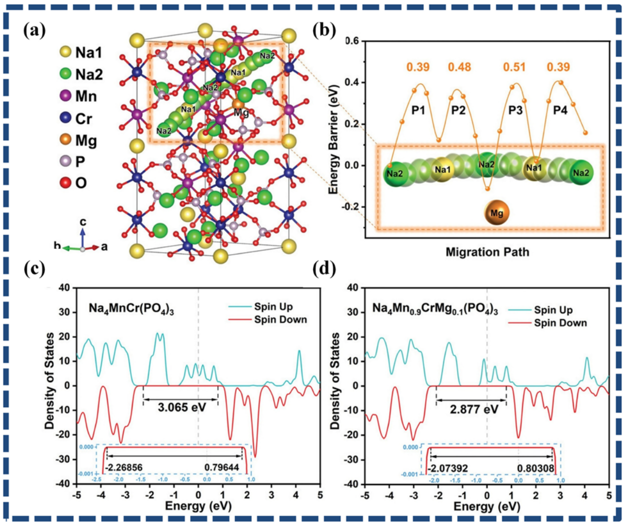

Fig. 7 (a) Schematic illustration of the favorable Na^+ migration pathways and (b) corresponding migration energy barriers in the $Na_4Mn_{0.9}CrMg_{0.1}(PO_4)_3$ framework. The total DOSs of (c) $Na_4MnCr(PO_4)_3$ and (d) $Na_4Mn_{0.9}CrMg_{0.1}(PO_4)_3$. Reproduced from ref. 98 with permission from Wiley, copyright 2022.

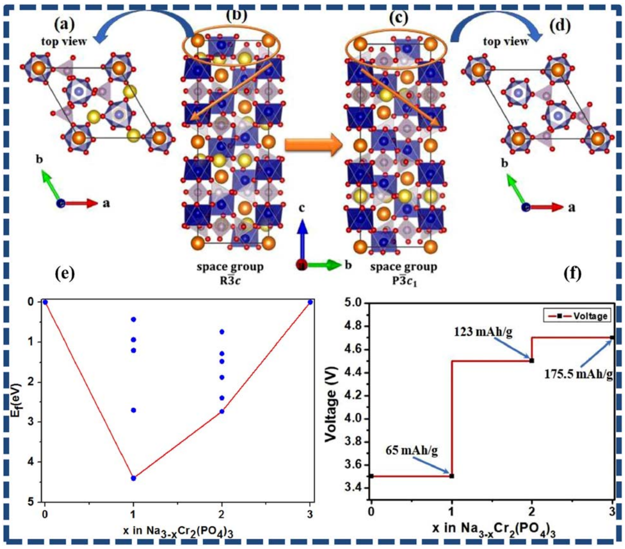

Fig. 8 Phase change and formation of a superstructure during desodiation (a) top view of $Na_3Cr_2(PO_4)_3$, (b) $Na_3Cr_2(PO_4)_3$ with space group $R\bar{3}c$, (c) superstructure of $Na_2Cr_2(PO_4)_3$ with space group $P\bar{3}c_1$, (d) top view of the superstructure of $Na_2Cr_2(PO_4)_3$, (e) the convex hull plot demonstrating the formation energies at different x values in $Na_{3-x}Cr_2(PO_4)_3$, and (f) a simulated voltage profile for the charging process of $Na_{3-x}Cr_2(PO_4)_3$ with equivalent specific capacities. Reproduced from ref. 105 with permission from Elsevier, copyright 2021.

In contrast, Zhu *et al.*[102] co-doped Cr and Ti into manganese phosphate-based NASICON materials to prepare materials with the chemical formula $Na_{3.5}MnCr_{0.5}Ti_{0.5}(PO_4)_3$ (NMCTP). The Na^+ migration barrier of the material was calculated by first principles calculations, and the results demonstrated that the highest migration barrier of NMCTP was 0.314 eV, which was lower than that of the comparable $Na_4MnCr(PO_4)_3$ (0.39 eV) and $Na_4Mn_{0.9}CrMg_{0.1}(PO_4)_3$ (0.51 eV) materials.[98] The favourable migration kinetics also permitted the assembled NMCTP@C//Sb@C full cell to demonstrate a high energy density of 421 W h kg^{-1}, based on the cathode material.

3.1.4 Other NASICON cathode materials. $Na_3Cr_2(PO_4)_3$ (NCP) is another NASICON cathode material. In comparison to NVP, they exhibit an identical structural configuration, both belonging to the $R\bar{3}c$ space group and exemplifying the typical NASICON structure.[103] Nevertheless, the $Cr^{3+/4+}$ redox pair in NCP offers a working potential of up to 4.5 V and a higher reversible capacity (79 mA h g^{-1}).[104] Mamoor *et al.*[105] employed DFT to investigate the crystal structure, electronic structure, and ion migration kinetics of NCP. It was observed that a crystal transformation (space group $R\bar{3}c \rightarrow P\bar{3}c_1 \rightarrow R\bar{3}c$) was occurring during the sodium removal process of NCP, as visualised in Fig. 8(a)–(d). This transformation was accompanied by a partial decrease in volume, which was attributed to the structural perturbation caused by the low electronegativity of Cr. The formation energy convex hulls (Fig. 8(e)) indicate that both Na_2CP and Na_1CP are thermodynamically stable phases. The sodium removal voltage diagram, as illustrated in Fig. 8(f), indicates that the initial sodium removal voltage of NCP is 3.65 V, the second sodium deintercalation voltage is 4.5 V, and the third is 4.7 V. Concurrently, the redox centre in the process of sodium removal was examined through a combination of density of states and Bader charge analysis. The analysis demonstrated that upon the removal of Na^+, the charge was transferred to the adjacent O atom, thereby facilitating the formation of a PO_4 tetrahedron.

Concurrently, Cr^{3+}, functioning as the redox centre lost the electronic equilibrium charge, resulting in the production of Cr^{4+}. The 3d orbital of Cr and the 2p orbital of O underwent hybridization, leading to the formation of a strongly bonded Cr–O bond. Ultimately, a P–O–Cr bond was established. The ion migration process of NCP was calculated by the CI-NEB method. It was found that the ion migration path was zigzag and the migration barrier was low (less than 0.5 eV), confirming the favourable ion migration performance of NCP. First-principles calculations confirm that NCP is an effective cathode material for sodium ion batteries.

Taveri *et al.*[106] studied the effect of Al substitution at the Fe-site in the NASICON cathode material $Na_3Fe_2(PO_4)_3$. The EIS test revealed that Al doping can markedly enhance the ionic conductivity of the material. A combination of XRD and DFT calculations revealed that although Al doping of $Na_3Fe_2(PO_4)_3$ reduced the cell volume, it released the migration path of $Na_3Fe_2(PO_4)_3$ and enlarged the bottleneck during Na^+ migration. Concurrently, DFT was employed to calculate the free energy, formation energy, and binding energy of $Na_3Al_xFe_{2-x}(PO_4)_3$ with varying crystal structures. The findings indicate that Al-doped $Na_3Fe_2(PO_4)_3$ exhibits a proclivity towards forming a monoclinic phase structure, which is also more conducive to ion migration. However, the actual performance of $Na_3Fe_2(PO_4)_3$ is suboptimal. The working potential is only 2.5 V, the specific capacity is 25 mA h g^{-1} at 0.1C, and it is only increased to 48 mA h g^{-1} after Al doping. Therefore, $Na_3Fe_2(PO_4)_3$ cannot be used as an effective cathode material for sodium ion batteries.

Additionally, $NaVPO_4F$ exhibits structural and redox potential similarities to NVP, along with a higher theoretical capacity (142 mA h g^{-1}). As a cathode material for sodium-ion batteries, $NaVPO_4F$ exhibits an exceptionally high potential; however, its low electronic conductivity restricts its practical applications.[107] The researchers employed a combination of first-principles calculations[108–110] and various experimental methods[111,112] to investigate the structure of the material. Aksyonov *et al.*[113] employed first-principles calculations to investigate the ion migration process of $AVPO_4F$ (A = Li, Na, K). Their findings revealed that despite the ionic radius of Na^+ and K^+ being larger than that of Li^+, the ion migration barrier of Na^+ and K^+ is equal to that of Li^+, suggesting that $NaVPO_4F$ exhibits enhanced ion diffusion capabilities. Mamoor *et al.*[110] studied the structural changes, charge transfer and kinetic properties of $NaVPO_4F$ during the sodium removal process. It was determined that the sodium removal process was accompanied by an 11% volume change, and that an intermediate phase was present during the sodium removal process. The sodium removal potential was 4.0 V, accompanied by a redox reaction involving the oxidation and reduction of $V^{3+/4+}$. The kinetic study demonstrated that the minimum migration barrier of $NaVPO_4F$ was 0.85 eV. Concurrently, the practical performance of $NaVPO_4F$ is commendable, with an actual working potential reaching 3.5 V, a specific capacity of 117 mA h g^{-1} at a 0.1C rate, and an enhanced capacity of 121.3 mA h g^{-1} following V-site Cr doping. These observations substantiate that $NaVPO_4F$ is a cathode material with a high working potential and commendable electrochemical performance.

3.1.5 Summary.

Tables 4 and 5 present an overview of the current research progress on NASICON materials, which has been achieved through the integration of computational and experimental studies. Of particular note are the studies on NVP and NVPF. These materials have been the subject of early-stage first-principles calculations and experimental investigations, aimed at exploring the effects of doping on the electronic conductivity of materials. This focus has been driven by their structural characteristics and the pioneering nature of the research.

The working potential of NVP is approximately 3.4 V, with a specific capacity of approximately 110 mA h g^{-1} at a 1C rate. However, the high band gap restricts the electrochemical performance. At present, the ion doping modification of NVP has been studied using both DFT and experimental methods. The doping sites include the Na, V and P sites, with the V site having been the subject of the most extensive study. A variety of elements, including Al, Ga, Ti, Mg, Mn, Cu, Fe, Zn, Nb, Co and Mo, have been employed for doping at the vanadium site. The Na site is primarily doped with K and Li within the same family, while the P site is doped with B. The electrochemical performance can be enhanced through doping. As an illustration, doping the material with Ti, Mg, Fe, Zn, and Mo at the V-site and Li at the Na-site can markedly enhance its rate performance, exceeding 80 mA h g^{-1} at a 10C rate. Similarly, doping the material with Mn and Nb at the V-site can significantly improve its cycle stability, with a capacity retention of over 85% after 1000 cycles.

The voltage platform of NVPF is higher, situated at approximately 3.7 V, and the specific capacity is comparable to that of NVP. Currently, it is also extensively employed in DFT doping research. The primary doping sites are those of Na and V, with doping elements including K, Cr, Ti, Fe, W, Al, Nb and Mo. The

Table 4 A first-principles computational modification study of $Na_3V_2(PO_4)_3$

		Band gap (eV)		Na-ion migration energy barriers (eV)		Voltage plateau (V)		Capacity (mA h g^{-1})		Capacity retention		
Doped site	Doped element	Undoped	Doped	Undoped	Doped	Undoped	Doped	Undoped	Doped	Undoped	Doped	Ref.
V	Al	1.735	1.580	0.477	0.547	3.4	3.4 3.9	110 (1C)	117.1 (1C)	70% (100)	95% (100)	69
	Ga					1.6 3.4	1.6 3.4 4.0	160 (1C)	152.3 (1C)	67% (70)	90% (70)	73
	Ti	1.08	0.94	0.42	0.35	3.4	3.4	40 (10C)	101.2 (10C)	0 (25)	86% (500)	70
	Mg							88.8 (10C)	96.7 (10C)	70.9% (180)	88.9% (180)	114
	Mn			0.342	0.309	3.4	3.43	108.6 (1C)	96.6 (1C)		87.2% (4000)	76
	Mn, Cu		0			3.4	3.4 3.6		79 (30C)		86.1% (3000)	115
	Fe					3.5	3.5	31.4 (20C)	91.16 (20C)	22.3% (100)	88.7% (100)	116
	Zn	1.51	0.56	0.457	0.402	3.4	3.4	45 (15C)	95.8 (15C)		90.7% (500)	75
	Nb	1.51	0.72	0.46	0.43	3.4	3.4	73.7 (2C)	107.9 (2C)	78.6% (500)	89.4% (1000)	71
	Co	3.01	1.41	0.42	0.39	3.4	3.4	63.7 (1C)	104.6 (1C)	93.1% (200)	95.7% (200)	72
	Mo			0.395	0.312	3.4	3.4	76.8 (10C)	92.1 (10C)	13% (500)	81% (500)	74
Na	Li					3.4	3.4	80 (20C)	102 (20C)			77
	K	5.80	4.88			3.4	3.4	106 (0.2C)	108.3 (0.2C)	78% (300)	95% (300)	79
P	B	2.7	1.633	0.396	0.282	3.4	3.4	82 (5C)	100 (5C)	91.8% (200)	98.7% (200)	81

Table 5 A first-principles computational modification study of NASICON materials

Materials	Doped site	Doped element	Band gap (eV)		Na-ion migration energy barriers (eV)		Voltage plateau (V)		Capacity (mA h g^{-1})		Capacity retention		Ref.
			Undoped	Doped	Undoped	Doped	Undoped	Doped	Undoped	Doped	Undoped	Doped	
$Na_3V_2(PO_4)_2F_3$	Na	K	2.75	2.68	0.187	0.128	3.43 3.76 4.23	3.43 3.76 4.23	110.6 (0.1C)	120.8 (0.1C)	78% (500)	97.5% (500)	87
		Cr	3.31	1.35			3.7 4.2	3.7 4.2	104.2 (1C)	117.7 (1C)	82.7% (200)	83.2% (200)	85
		Ti	1.167	1.049			3.4 3.7 4.2	3.4 3.7 4.2	60 (40C)	104.2 (40C)			88
	V	Fe	4.47	3.79			3.7 4.2	3.7 4.2		126.7 (0.1C)		97.1% (100)	89
		W	4.02	1.35						159.7 (0.1C)		87.7% (100)	90
		Al	1.951	1.862			3.4 3.7 4.2	3.4 3.7 4.2	72 (5C)	87 (5C)	71.8% (400)	74.4% (400)	91
		Mo			0.647	0.27	3.24 3.6 4.53	2.64 3.6 3.94					92
$Na_4MnCr(PO_4)_3$	Mn	Mg	3.065	2.887	0.39	0.51	3.5 4.1 4.35	3.5 4.2	130 (C/20)	154.6 (0.1C)	88% (20)	84.8% (50)	98
	Cr	Ti	3.065		0.39	0.314	3.5 4.1 4.35	2.5 3.5 4.1 4.35	130 (C/20)	160.4 (C/20)	88% (20)	94.2% (50)	117
$Na_3Cr_2(PO_4)_3$			1.0		0.42		3.65 4.5 4.7		123				105
$Na_3Fe_2(PO_4)_3$	Fe	Al					2.5	2.5	25 (0.1C)	48 (0.1C)			106
$NaVPO_4F$	V	Cr					3.5	3.5	117 (1C)	121.3 (1C)			110
$Na_3Ti_2(PO_4)_3$	$[PO_4]$	F	2.624	1.039			2	2	72.2 (1C)	125.7 (1C)	35.4% (2000)	75.5% (2000)	118
$NaV_3(PO_4)_3$							1.18	0.85	177	208			119

conductivity of the material is enhanced by ion doping, which also improves its electrochemical performance. In particular, the V-site Ti doping exhibits enhanced performance (specific capacity increased by 40 mA h g^{-1} at 40 °C), while the Na-site K doping cycle demonstrates superior stability (capacity retention rate reaching 97.5% after 500 cycles).

Manganese phosphate-based NASICON materials exhibit high working potentials (on average above 3.5 V) due to the $Mn^{2+}/Mn^{3+}/Mn^{4+}$ redox pair. Among these materials, $Na_3CrMn(PO_4)_3$ and $Na_3MnTi(PO_4)_3$ have attracted particular attention due to their high capacity. Nevertheless, analogous to other Mn-based materials, the Jahn–Teller effect of Mn^{3+} engenders pronounced structural perturbations and constrains the cycling and multiplicity properties of the materials. Furthermore, the internal antisite defects introduced during the synthesis process further compromise the kinetic properties. Consequently, ion doping has also been employed as a means of enhancing the structural stability of the materials. The introduction of Mg^{2+} and Mo^{3+} as doping ions into NCMP and NMTP has been demonstrated to effectively enhance the charge/discharge capacity of the materials. However, the cycling and multiplicity performances of the materials remain suboptimal, underscoring the continued necessity for the exploration of novel methods to optimise their performance.

There is a paucity of research on NCP, $Na_3Fe_2(PO_4)_3$ and $NaVPO_4F$. The electrochemical properties of NCP and $NaVPO_4F$ are analogous to those of NVP, and the specific capacity of the material can be enhanced through doping. However, $Na_3Fe_2(PO_4)_3$ exhibits suboptimal performance and is challenging to utilise as a cathode material for sodium ion batteries. NCP and $NaVPO_4F$ demonstrate considerable potential for commercial application, yet they remain inferior to commercial lithium ion battery materials. Consequently, further investigation into techniques such as multi-ion doping and carbon-based material coating is essential to enhance the electrochemical performance of these materials.

3.2 NASICON anode materials

3.2.1 $Na_3Ti_2(PO_4)_3$. The structure of $Na_3Ti_2(PO_4)_3$ (NTP) is also that of a NASICON, comprising TiO_6 octahedra and PO_4

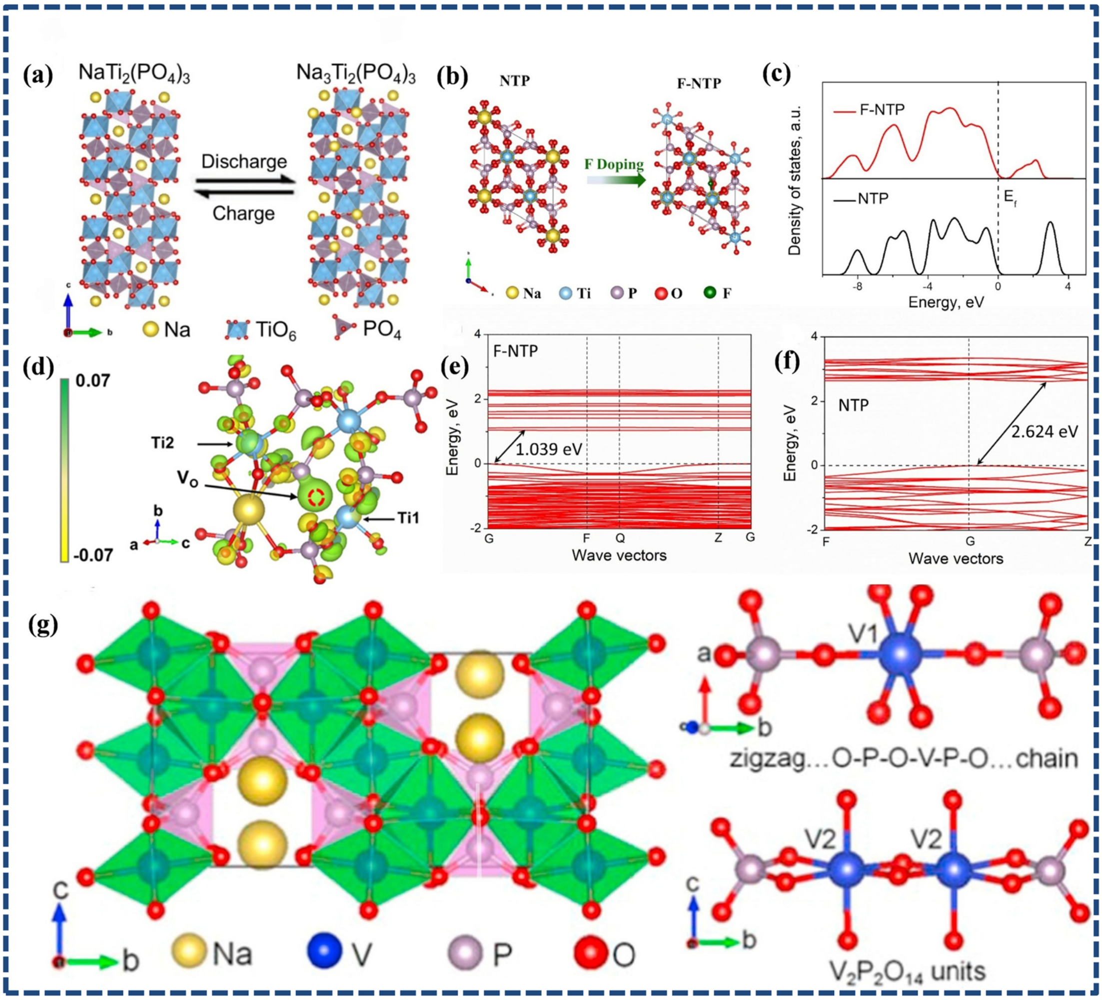

Fig. 9 (a) Schematic illustrations of the Na^+ storage mechanism upon the charge and discharge process in NTP. Reproduced from ref. 118 with permission from Elsevier, copyright 2022. (b) Structural illustration of F-NTP. (c) DOS of NTP and F-NTP, where the Fermi level is selected to be 0 eV. (d) The 2D charge density difference from the [−1.5 2.5 7.2] plane. Reproduced from ref. 121 with permission from the Royal Society of Chemistry, copyright 2024. The band structure of (e) F-NTP and (f) NTP. Reproduced from ref. 118 with permission from Elsevier, copyright 2022. (g) Schematic illustrations of $NaV_3(PO_4)_3$. Reproduced from ref. 119 with permission from Elsevier, copyright 2016.

tetrahedra linked by O-sharing to create a distinctive lantern unit, with Na^+ occupying the interstitial space.[120] Senguttuvan *et al.*[120] calculated the average sodium insertion potential of NTP by first-principles calculation and compared the results with the experimental data. The sodium insertion process potential from Na_1TP to Na_3TP, as displayed in Fig. 9(a), was determined to be 2.12 V. Additionally, the sodium insertion process potential from Na_3TP to Na_4TP was found to be 0.36 V, which aligns with the experimental outcomes. Concurrently, the sodium insertion process is accompanied by the redox process of $Ti^{2+/3+/4+}$. It is postulated that NTP can be employed as a low-voltage electrode material and is suitable as a negative electrode material.

However, as a typical NASICON material, the NTP material exhibits poor electronic conductivity. In order to enhance the conductivity of the material, DFT-assisted ion doping is also employed in the investigation of battery materials. He *et al.*[122] prepared a coating of NTP doped with N-doped carbon nanofibres. A DFT calculation revealed that the valence band electrons of NTP coated with N-doped carbon nanofibers crossed the Fermi level to the conduction band, indicating that the material had undergone a transformation into a conductor at this point in time. The calculation of the Na^+ migration energy barrier also demonstrates that the Na^+ migration barrier of N–C coated NTP at the interface between the N–C coating layer and NTP is reduced, thereby improving the ionic conductivity. The experimental study also demonstrates that the electrochemical performance of the material is enhanced at this juncture. Deng *et al.*[118] enhanced the electronic conductivity of the material through a straightforward F doping process (Fig. 9(b) and (c)). The results of the band structure calculation indicated that F doping can reduce the band gap value of the material from 2.624 eV (Fig. 9(f)) to 1.039 eV (Fig. 9(e)). Experimental studies have demonstrated that the material exhibits favourable rate performance (108.7 mA h g^{-1} at a 50C rate) and cycle life (75.5% capacity retention after 2000 charge and discharge cycles at a 10 °C rate). It is also crucial to consider the battery material's performance at low temperatures. Furthermore, the use of DFT calculations has been demonstrated to enhance the low-temperature performance of NTP materials. Li *et al.*[123] enhanced the low-temperature performance of NTP nanocrystals by modifying NTP nanocrystals with flake carbon, achieving a specific capacity of 94.3 mA h g^{-1} after 200 cycles at a discharge rate of 0.5 A g^{-1} at −25 °C. DFT calculations of sodium adsorption energy and density of states demonstrate that the advancement in material performance is attributable to the enhancement of electronic conductivity and diffusion efficiency resulting from the robust interconnection between the carbon layer and NTP. Wang *et al.*[121] employed defect engineering techniques to synthesise oxygen-rich vacancy core–shell $C@NaTi_2(PO_4)_{3-x}$ composites. The calculation of the electron local density difference, as illustrated in Fig. 9(d), demonstrates that the incorporation of oxygen vacancies results in the localised electron concentration of neighbouring Ti and P atoms in proximity to the Fermi level, thereby reducing the material's band gap. Concurrently, the absence of O atoms facilitates the diffusion and migration of Na^+. Moreover, experimental investigations have substantiated that the electrochemical performance of the material is enhanced.

3.2.2 $NaV_3(PO_4)_3$. Given its structural similarity to NVP, $NaV_3(PO_4)_3$ is regarded as a prospective anode material for sodium ion batteries, largely on account of its comparatively low sodium ion release potential. Hu *et al.*[119] employed the sol–gel method to synthesise this material and utilised the XRD Rietveld refinement technique to examine its structure. The results indicate that the material exhibits an α-$CrPO_4$ structure, with the diffraction peak pointing to the *Imma* space group. These two vanadium sites are connected by corner-shared oxygen atoms to form a framework with larger cavities and tunnels, which provide storage sites and migration channels for sodium atoms (Fig. 9(g)). The two V sites are linked by corner-shared O atoms to form a framework with larger cavities/tunnels, which serve as storage sites and migration channels for Na atoms. Concurrently, the XRD patterns of $NaV_3(PO_4)_3$ with varying Na concentrations were obtained using first-principles calculation. The findings indicate that Na^+ occupies the 4*e* site in $NaV_3(PO_4)_3$, and that Na^+ initially occupies the 4*b* site and subsequently the 4*c* site during the sodium insertion process. This results in a volumetric expansion of the material, with a maximum expansion rate of 10.9%.

In their study, Wang *et al.*[124] employed first-principles calculations to investigate the electrochemical reaction mechanism and structural evolution of $NaV_3(PO_4)_3$ anode materials. The calculation of the density of states indicates that $NaV_3(PO_4)_3$ is a semiconductor material with a band gap of 1.032 eV. The energy band near the Fermi level is primarily occupied by the 3d electrons of V, accompanied by the insertion of Na^+ and the reduction of V^{3+} to V^{2+}. This gradual increase in the band gap limits the electrochemical performance of the material. Additionally, it was observed that the Na^+ migration energy barrier of $NaV_3(PO_4)_3$ was considerably higher than that of $Na_{1.125}V_3(PO_4)_3$, which further substantiated the favourable structural stability of the material. The experimental findings of Feng *et al.*[125–127] also corroborated this conclusion. Nevertheless, the intrinsic low electronic conductivity and restricted ion mobility of the material also restrict its electrochemical performance. At present, ion doping[126,127] and nano-engineering[125] have also been employed for $NaV_3(PO_4)_3$, which has resulted in an enhancement of the electrochemical performance of the material. The nano-carbon-coated $NaV_3(PO_4)_3$ voltage platform exhibited a reduction in voltage from 1.18 V to 0.85 V, accompanied by an increase in maximum discharge capacity from 177 mA h g^{-1} to 208 mA h g^{-1} at a discharge rate of 75 mA g^{-1}. The complete battery, comprising a $Na_3V_2(PO_4)_3$ cathode, is capable of delivering a capacity of 140 mA h g^{-1} at an average operating voltage of 1.8 V and a discharge rate of 750 mA g^{-1}.

3.2.3 Summary. In order to gain insight into the electrochemical reaction mechanism and enhance the electronic conductivity of the anode materials $Na_3Ti_2(PO_4)_3$ and $NaV_3(PO_4)_3$, first-principles calculations have been employed. This approach has been complemented by doping modifications of the materials. Table 5 illustrates that the working potential of NTP is 2 V, and the specific capacity is relatively low.

Table 6 Comparison of sodium-ion solid electrolytes

Material	Ion conductivity (mS cm^{-1})	Electrochemical stabilization window (V)	Preparation condition	Ref.
$Na_{1-x}Zr_xLa_{1-x}Cl_4$	0.29	1.33–3.8	Easier	136
$Na_{2.7}ZrCl_{5.3}O_{0.7}$	0.229	1.5–3.5	Normal	137
$Na_{2.895}W_{0.3}Sb_{0.7}S_4$	14.5	0.8–2.8	Harder	138
Na_3BS_3	0.1	1.5–3.0	Harder	139
PEO/NaTFSI/HAP	0.1	1–5.1	Normal	140
Na_3YBr_6	4.57×10^{-5}	1.43–3.35	Easier	141
NAS-WCl_6-Na_3SbS_4	6.4	0.6–2.8	Normal	142
$Na_3Zr_2Si_2PO_{12}$	3.49	2–5	Normal	143

Conversely, $NaV_3(PO_4)_3$ exhibits a lower working potential and higher specific capacity, which enhances the material's commercial potential as an anode. Nevertheless, it remains inferior to existing carbon anode materials. Further research is essential to enhance the specific capacity and cycle stability of the material.

3.3 NASICON electrolyte materials

As a crucial component of battery materials, electrolyte materials exert a significant impact on the performance of sodium-ion batteries. Solid electrolyte materials, which offer enhanced safety compared to traditional liquid electrolytes, have garnered significant attention, particularly fast ionic conductor materials with excellent and high ionic conductivity. In light of the current research, fast ionic conductors can be classified into four main categories: polymer-based, oxy, sulfide-based and halide-based electrolytes.[128,129] Currently the lower room temperature ionic conductivity (<1 mS cm^{-1}) of polymer-based electrolytes and halides,[130] the restricted electrochemical stabilisation window of sulphide-based electrolyte materials, and stringent preparation issues (stemming from the poor air stability of sulphides)[131–135] are limiting the development of solid-state electrolyte materials, as shown in Table 6. Among the most mature oxy-electrolytes, the commercially applied high-temperature electrolyte material β-alumina is also difficult to be directly applied in solid-state electrolytes for sodium-ion battery materials due to its low ionic conductivity at room temperature.[144] Therefore, it is of great importance to investigate solid-state electrolyte materials with higher room-temperature ionic conductivity and stability. As a representative example of oxygen-based electrolyte materials, the open and stable three-dimensional skeleton structure of phosphate-based NASICON materials endows them with superior room-temperature ionic conductivity (>1 mS cm^{-1}), enhanced chemical and thermal stability, and augmented mechanical strength when compared to other sulfide, halide, and solid-state electrolyte materials.[145,146] Consequently, they are employed in the development of solid-state electrolyte materials for sodium-ion batteries.

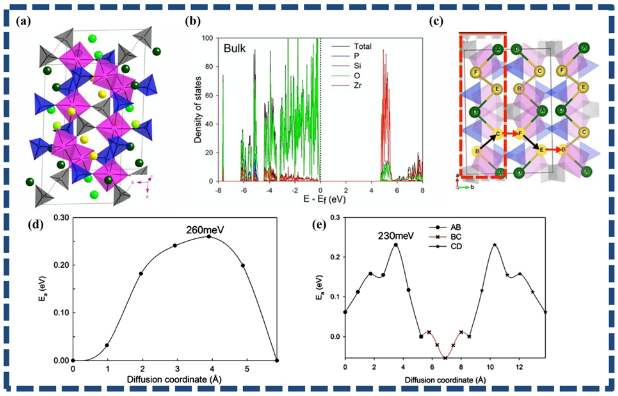

Fig. 10 (a) The crystal structure of $Na_3Zr_2Si_2PO_{12}$. Na at the Na[1] site is shown by yellow balls, Na at the Na[2] site by light green balls, and Na at the Na[3] site by dark green balls. The Zr octahedra are shown in pink, the Si tetrahedra in blue, and the P tetrahedra in grey; (b) the density of states for the bulk $Na_3Zr_2Si_2PO_{12}$; (c) schematic of the Na diffusion chain. The black and red arrows indicate the inner-chain processes and inter-chain processes, respectively; (d) activation energies of Na vacancy diffusion along the inter-chain process; (e) activation energies of Na vacancy diffusion along processes AB, BC, and CD. The circle, cross, and star symbols represent the activation energy profile of the processes AB, BC, and CD, respectively. Reproduced from ref. 147 with permission from the Royal Society of Chemistry, copyright 2016.

The Zr-based NASICON material $Na_3Zr_2Si_xP_{3-x}O_{12}$ ($0 \le x \le 3$) is currently the subject of significant research, and first-principles calculations are also employed in the study of solid electrolytes. Bui *et al.*[147] conducted a study of the crystal structure, electronic structure and ion diffusion mechanism of $Na_3Zr_2Si_2PO_{12}$ based on density functional theory. As illustrated in Fig. 10(a), $Na_3Zr_2Si_2PO_{12}$ is a representative NASICON structure, belonging to the $C2/c$ monoclinic space group. The $[ZrO_6]$ octahedron is connected to the $[PO_4]$ tetrahedron and the $[SiO_4]$ tetrahedron by corner-sharing O atoms, resulting in each $[PO_4]$ tetrahedron or $[SiO_4]$ tetrahedron being linked to four $[ZrO_6]$ octahedra, thereby forming a distinctive hexagonal bottleneck structure. This provides a storage location and migration path for Na^+. The electronic density of states calculation indicates that $Na_3Zr_2Si_2PO_{12}$ is an insulator-like material with a band gap of 4.6 eV. The valence band is predominantly populated by the 2p orbital of oxygen, while the conduction band is primarily composed of 3d electrons from Zr. The 3d state of Zr and the 2p orbital of O exhibit a high degree of localisation (Fig. 10(b)). The investigation into the diffusion mechanism reveals that Na^+ migration encompasses three intra-chain diffusion processes and a single inter-chain diffusion process, as illustrated in Fig. 10(c). When Na is situated within the chain, it predominantly migrates along the Na diffusion chain. Conversely, when Na is positioned inter-chain, it primarily migrates through the Na diffusion chain. The diffusion barriers for these two processes are 0.23 eV (Fig. 10(e)) and 0.26 eV (Fig. 10(d)), respectively, with the ionic conductivity being superior.

In their study, Park *et al.*[148] investigated the impact of Na excess on the sodium ion diffusion properties of $Na_3Zr_2Si_2PO_{12}$. A combination of experimental and theoretical approaches revealed that the diffusion of the material can be divided into two distinct aspects: the grain boundary and grain. The separation and quantification of the intrinsic conductivity demonstrate that the decisive factor governing the ionic conductivity is the grain diffusion at low temperature (100 °C). The introduction of excess Na^+ has the potential to enhance grain diffusion by increasing the minimum bottleneck size of the Na^+ migration channel. Conversely, it may also lead to a reduction in the effective carrier concentration within the material, which could subsequently diminish the conductivity of the material. However, it was discovered that the ionic conductivity of the Na^+ excess sample at 300 °C was 0.12 S cm^{-1}, which was approximately 92% higher than that of the pure sample. The first-principles calculation verified that the enhancement in the ionic conductivity of the material was predominantly attributable to the increase in grain diffusion resulting from the presence of excessive Na^+. Consequently, the high-temperature ionic conductivity of the material can be enhanced by the introduction of excess Na^+.

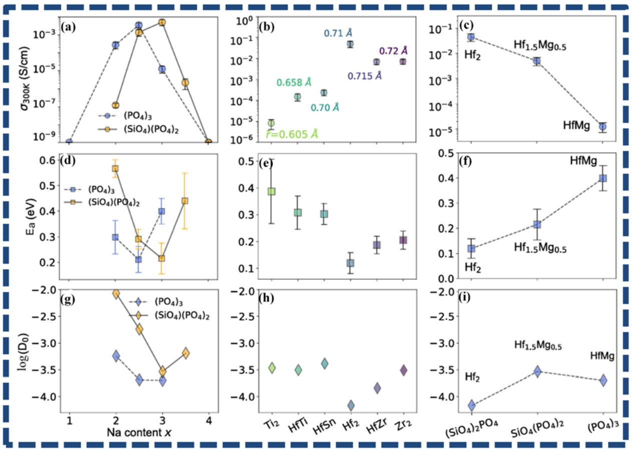

Fig. 11 Bulk ionic conductivities, activation energies, and prefactors calculated by AIMD. Calculated room-temperature (300 K) bulk ionic conductivities (a) and activation energies (d) with error bars, and prefactors (g) of $Na_{1+2y}Hf_{2-y}Mg_yP_3O_{12}$ ($y = 0, 0.5, 0.75, 1, 1.5$, labeled blue) and $Na_{2+2z}Hf_{2-z}Mg_zSiP_2O_{12}$ ($z = 0, 0.25, 0.5, 0.75, 1$, labeled yellow). In these two groups, both the polyanion composition and cation radius are kept constant. Note that for compounds with $y = 0$, 1.5 and $z = 1$, the conductivities were not converged and therefore set as $\ll 10^{-9}$ mS cm^{-1}. (b, e, and h) Group of $Na_3MM'Si_2PO_{12}$ (M, M′ = Ti, Hf, Sn, Zr), with constant Na content x and polyanion composition. (c, f and i) Group of $Na_3Hf_{2-z}Mg_zSi_{2-2z}P_{1+2z}O_{12}$ ($z = 0, 0.5, 1$) where r_M and the Na content x are kept constant. Reproduced from ref. 150 with permission from Springer Nature, copyright 2023.

In order to enhance the ionic conductivity of Na^+, Wang *et al.*[149] investigated the impact of incorporating Na_2SiO_3 on the ionic conductivity of $Na_3Zr_2Si_2PO_{12}$, discerning that the introduction of Na_2SiO_3 can diminish the requisite temperature for $Na_3Zr_2Si_2PO_{12}$ prepared through liquid phase sintering. The addition of Na_2SiO_3 has been demonstrated to reduce the migration barrier (diffusion barrier 0.21 eV) and improve the ionic conductivity of the material (ionic conductivity 1.28 mS cm^{-1}) through DFT calculations.

In contrast, Wang *et al.*[150] examined the impact of NASICON anion species and quantity on the ionic conductivity of NASICON solid-state electrolytes in another study. Initially, eight NASICON materials that were phase-stable were selected through the application of high-throughput density flooding theory calculations in conjunction with the specified preparation conditions. Subsequently, the activation energies, migration coefficients and ionic conductivities of these NASICON materials with different anionic and cationic compositions were calculated by AIMD. This enabled the assessment of the effects of each anionic and cationic composition and content on the diffusion kinetics of the materials. As illustrated in Fig. 11, the findings of the AIMD calculations suggest that the optimal Na content of NASICON materials is approximately $x = 3$. However, this is subject to variation depending on the anionic species and content. NASICON materials that feature larger cations and a high silicate content tend to exhibit enhanced ionic conductivity. The final experimental synthesis resulted in the preparation of $Na_{3.4}Hf_{0.6}Sc_{0.4}ZrSi_2PO_{12}$, which exhibited an ionic conductivity of up to 1.2 mS cm^{-1}.

Tieu *et al.*[143] synthesised a zirconia-free $Na_3Zr_2Si_2PO_{12}$ material in view of the low ionic conductivity of zirconia. The zirconia-free $Na_3Zr_2Si_2PO_{12}$ was confirmed through a combination of techniques, including synchrotron radiation X-ray diffraction, Raman spectroscopy and density functional theory simulation. Impedance spectroscopy measurements demonstrated that the total ionic conductivity at room temperature was 3.49 mS cm^{-1}, with a volume conductivity of 10.05 mS cm^{-1}. Nevertheless, the present NASICON solid-state electrolyte remains inadequate for the requirements of electrolyte materials for commercial large-scale energy storage batteries. Consequently, there is a need to investigate methods for enhancing its ionic conductivity.

4. Conclusions

Presently, first-principles calculations are employed to ascertain the intrinsic properties of NASICON materials. The intrinsic properties of NASICON cathode materials ($Na_3V_2(PO_4)_3$, $Na_3V_2(PO_4)_2F_3$, $Na_3Cr_2(PO_4)_3$, $Na_3Fe_2(PO_4)_3$, and $NaVPO_4F$), anode materials ($Na_3Ti_2(PO_4)_3$ and $NaV_3(PO_4)_3$) and electrolyte materials ($Na_3Zr_2Si_2PO_{12}$) have been calculated and studied. The results of the calculations demonstrate that these materials exhibit excellent structural stability, which is conferred by the NASICON structure. Furthermore, they display favourable operating voltages, with the cathode material operating at approximately 2 to 4.2 V and the anode material operating below 2 V. Additionally, they exhibit exceptional sodium ion transport performance, with the Na^+ migration barrier being less than 1 eV. These properties indicate significant potential for their application.

Concurrently, the NASICON structure also results in diminished electronic conductivity of the material, which constrains the electrochemical functionality of the material. Accordingly, single ion doping in conjunction with DFT calculations is employed in the investigation of enhanced material conductivity. To achieve this, first-principles calculations have been employed to successfully identify materials that enhance the electronic conductivity of NASICON materials, thus greatly reducing the time required for experimental research. Nevertheless, the electrochemical performance of NASICON materials remains inferior to that of commercial lithium-ion battery materials. It is therefore evident that further study is required on multi-ion doping, carbon-based material coating, material nano-engineering and other methods with a view to improve the electrochemical performance of materials. Furthermore, the high cost of computer technology and computing software means that DFT calculations cannot fully realise their potential in simplifying experimental research, which in turn limits the application of DFT calculations.

5. Application prospects of first-principles calculation in NASICON materials

In the realm of phosphate-based NASICON battery materials, first-principles calculations have been employed to ascertain the intrinsic properties of materials and to investigate the effects of element doping. Nevertheless, at this time, it is primarily employed as an experimental auxiliary tool to investigate the mechanism of material performance optimisation. Consequently, first-principles calculations are unable to fully realise their potential in simplifying the experimental process. Furthermore, the dearth of first-principles calculation data and the discrepancy in calculation standards for phosphate-based NASICON battery materials have also impeded the advancement of this field of research. It is therefore anticipated that the future application of first-principles calculations in NASICON battery materials will be as follows:

(1) Presently, research into ion doping of phosphate-based NASICON is primarily concerned with single ion doping. In the future, the potential for mixed ion doping can be investigated through the use of DFT calculations, with the aim of further enhancing the conductivity and electrochemical performance of materials.

(2) As computer technology and calculation software continue to advance, first-principles calculations will increasingly become the primary focus of research on NASICON cathode materials. The development of new NASICON materials may be informed by computational modelling. In particular, the impact of varying doping elements on the electronic structure, sodium removal potential and Na^+ migration barrier of NASICON can be evaluated through first-principles calculations. This approach enables the identification of elements that enhance the electronic conductivity of the material and achieve a balance between the sodium removal potential and Na^+ migration barrier. The electrochemical properties of the materials are tested through experimentation, and the research and development of new element-doped NASICON cathode materials are ultimately guided, which can significantly reduce the time required for research and development.

(3) The ongoing advancement of machine learning technology has led to its extensive utilisation in a multitude of research endeavours. Furthermore, machine learning has been employed in the investigation of lithium-ion battery materials, given its capacity to process intricate, extensive data sets, and has directed the advancement of several novel materials.[151,152] As a consequence of the ongoing expansion of both the theoretical calculations and empirical data pertaining to NASICON cathode materials, there is a growing recognition of the potential benefits to be gained from integrating machine learning, first-principles calculations and experimentation in the pursuit of new NASICON cathode materials. This represents a promising avenue of future research.

Data availability

The data that support the findings of this study are available from the corresponding author upon reasonable request.

Conflicts of interest

There are no conflicts to declare.

References

1 I. Zafar, V. Stojceska and S. Tassou, *Renewable Sustainable Energy Rev.*, 2024, **189**, 113962.
2 O. Omoyele, M. Hoffmann, M. Koivisto, M. Larrañeta, J. M. Weinand, J. Linßen and D. Stolten, *Renewable Sustainable Energy Rev.*, 2024, **189**, 113792.
3 A. A. Eladl, S. Fawzy, E. E. Abd-Raboh, A. Elmitwally, G. Agundis-Tinajero, J. M. Guerrero and M. A. Hassan, *Electr. Power Syst. Res.*, 2024, **226**, 109915.
4 Y. Zhao, Q. Liu, X. Zhao, D. Mu, G. Tan, L. Li, R. Chen and F. Wu, *Mater. Today*, 2023, **62**, 271–295.
5 G. Wei, Y. Liu, B. Jiao, N. Chang, M. Wu, G. Liu, X. Lin, X. Weng, J. Chen, L. Zhang, C. Zhu, G. Wang, P. Xu, J. Di and Q. Li, *iScience*, 2023, **26**, 107676.
6 K. Chayambuka, G. Mulder, D. L. Danilov and P. H. L. Notten, *Adv. Energy Mater.*, 2020, **10**, 2001310.
7 Nagmani, D. Pahari, P. Verma and S. Puravankara, *J. Energy Storage*, 2022, **56**, 105961.
8 Z.-Y. Gu, X.-T. Wang, Y.-L. Heng, K.-Y. Zhang, H.-J. Liang, J.-L. Yang, E. H. Ang, P.-F. Wang, Y. You, F. Du and X.-L. Wu, *Sci. Bull.*, 2023, **68**, 2302–2306.
9 T. Yu, G. Li, Y. Duan, Y. Wu, T. Zhang, X. Zhao, M. Luo and Y. Liu, *J. Alloys Compd.*, 2023, **958**, 170486.
10 K. Mathiyalagan, D. Shin and Y.-C. Lee, *J. Energy Chem.*, 2024, **90**, 40–57.

11 M. Mamoor, Y. Li, L. Wang, Z. Jing, B. Wang, G. Qu, L. Kong, Y. Li, Z. Guo and L. Xu, *Green Energy and Resources*, 2023, **1**, 100033.
12 X. Xiang, K. Zhang and J. Chen, *Adv. Mater.*, 2015, **27**, 5343–5364.
13 Y. Liu, C. Sun, Y. Li, H. Jin and Y. Zhao, *Energy Storage Mater.*, 2023, **57**, 69–80.
14 R. Thirupathi, V. Kumari, S. Chakrabarty and S. Omar, *Prog. Mater. Sci.*, 2023, **137**, 101128.
15 Q. Yang, Z. Li, H. Tian and Z. Su, *Ceram. Int.*, 2019, **45**, 6291–6295.
16 S. Qiu, X. Wu, M. Wang, M. Lucero, Y. Wang, J. Wang, Z. Yang, W. Xu, Q. Wang, M. Gu, J. Wen, Y. Huang, Z. J. Xu and Z. Feng, *Nano Energy*, 2019, **64**, 103941.
17 J. Wu, H. Liu, Y. Li and C. Zhang, *Chem. Commun.*, 2023, **59**, 8985–8988.
18 H. Tian, S. Liu, L. Deng, L. Wang and L. Dai, *Energy Storage Mater.*, 2021, **39**, 232–238.
19 B. Pandit, M. Johansen, B. P. Andersen, C. S. Martínez-Cisneros, B. Levenfeld, D. B. Ravnsbæk and A. Varez, *Chem. Eng. J.*, 2023, **472**, 144509.
20 J. M. Naranjo-Balseca, C. S. Martínez-Cisneros, B. Pandit and A. Várez, *J. Eur. Ceram. Soc.*, 2023, **43**, 4826–4836.
21 Y. Li, M. Li, Z. Sun, Q. Ni, H. Jin and Y. Zhao, *Energy Storage Mater.*, 2023, **56**, 582–599.
22 M. K. Chong, Z. Zainuddin, F. S. Omar and M. H. H. Jumali, *Ceram. Int.*, 2022, **48**, 22106–22113.
23 A. Chakraborty, R. Thirupathi, S. Bhattacharyya, K. Singh and S. Omar, *J. Power Sources*, 2023, **572**, 233092.
24 J. B. Goodenough, H. Y. P. Hong and J. A. Kafalas, *Mater. Res. Bull.*, 1976, **11**, 203–220.
25 H. Y. P. Hong, *Mater. Res. Bull.*, 1976, **11**, 173–182.
26 S.-J. Chiang, J. A. Kaduk and L. L. Shaw, *Mater. Chem. Phys.*, 2024, **312**, 128656.
27 S. Terny, C. López, G. Narda and M. A. Frechero, *Ceram. Int.*, 2022, **48**, 31755–31762.
28 X. Shen, M. Han, Y. Su, M. Wang and F. Wu, *Nano Energy*, 2023, **114**, 108640.
29 Y. Li, Q. Shi, X. Yin, J. Wang, J. Wang, Y. Zhao and J. Zhang, *Chem. Eng. J.*, 2020, **402**, 126181.
30 T. Xu, M. Zhao, Z. Su, W. Duan, Y. Shi, Z. Li, V. G. Pol and X. Song, *J. Power Sources*, 2021, **481**, 229110.
31 D. Wang, N. Su, Z.-E. Yu, S. Lu, Y. Lyu and B. Guo, *Electrochem. Commun.*, 2024, **159**, 107651.
32 J. Yang, J. Dai, D. Su, Q. Ren, G. Liu, Q. Luo, J. Luo, Z. Ye, H. Hai and L. Liu, *Appl. Surf. Sci.*, 2023, **608**, 154934.
33 H. Jiang and H.-Y. Sun, in *Quantum Chemistry in the Age of Machine Learning*, ed. P. O. Dral, Elsevier, 2023, pp. 27–65, DOI: 10.1016/B978-0-323-90049-2.00002-0.
34 Q. Bai, L. Yang, H. Chen and Y. Mo, *Adv. Energy Mater.*, 2018, **8**, 1702998.
35 A. Urban, D.-H. Seo and G. Ceder, *npj Comput. Mater.*, 2016, **2**, 1–13.
36 Y.-H. Chen, Y.-H. Zhao, S.-H. Tian, P.-F. Wang, F. Qiu and T.-F. Yi, *Composites, Part B*, 2023, **266**, 111030.
37 M. Aydinol, A. Kohan, G. Ceder, K. Cho and J. Joannopoulos, *Phys. Rev. B: Condens. Matter Mater. Phys.*, 1997, **56**, 1354.
38 R. J. Clement, D. S. Middlemiss, I. D. Seymour, A. J. Ilott and C. P. Grey, *Chem. Mater.*, 2016, **28**, 8228–8239.
39 W. Yang, Z. She, X. Wang, S. Lu, R. Zhao, X. Yang, Q. Wu, K. Shi, Y. Ruan and Q. Xie, *Surf. Interfaces*, 2024, **44**, 103787.
40 L. Lei, K. Sun, Z. Hongwei, C. Wang and T. Wei, *J. Energy Storage*, 2024, **78**, 109923.
41 Y. Cao, Y. Liu, D. Zhao, J. Zhang, X. Xia, T. Chen, L.-c. Zhang, P. Qin and Y. Xia, *J. Alloys Compd.*, 2019, **784**, 939–946.
42 S. Altundag, S. Altin, S. Yaşar and E. Altin, *Vacuum*, 2023, **210**, 111853.
43 X. Ge, X. Li, Z. Wang, H. Guo, G. Yan, X. Wu and J. Wang, *Chem. Eng. J.*, 2019, **357**, 458–462.
44 X. Li, Y. Shang, D. Yan, L. Guo, S. Huang and H. Y. Yang, *ACS Nano*, 2022, **16**, 453–461.
45 B. Xiang, J. Zhang, X. Zhang, W. Yan, J. Xu, J. Wang, H. Yu, L. Yan, L. Zhang and J. Shu, *Composites, Part B*, 2022, **246**, 110241.
46 G. Henkelman, A. Arnaldsson and H. Jónsson, *Comput. Mater. Sci.*, 2006, **36**, 354–360.
47 D. Sanchez-Portal, E. Artacho and J. M. Soler, *Solid State Commun.*, 1995, **95**, 685–690.
48 S. Wang, Y. Liu and Y. Mo, *Angew. Chem., Int. Ed.*, 2023, **62**, e202215544.
49 L. Xia, H. Liu, Y. Pei and L. Xia, *Nanoscale*, 2024, **16**, 15481–15501.
50 Y. Yang, C. Guan, R. Ouyang and H. Zhu, *Chem. Mater.*, 2024, **36**, 3776–3785.
51 S. Y. Lim, H. Kim, R. A. Shakoor, Y. Jung and J. W. Choi, *J. Electrochem. Soc.*, 2012, **159**, A1393.
52 Z. Jian, W. Han, X. Lu, H. Yang, Y.-S. Hu, J. Zhou, Z. Zhou, J. Li, W. Chen, D. Chen and L. Chen, *Adv. Energy Mater.*, 2013, **3**, 156–160.
53 S. Li, Y. Dong, L. Xu, X. Xu, L. He and L. Mai, *Adv. Mater.*, 2014, **26**, 3545–3553.
54 Z. Jian, C. Yuan, W. Han, X. Lu, L. Gu, X. Xi, Y. S. Hu, H. Li, W. Chen and D. Chen, *Adv. Funct. Mater.*, 2014, **24**, 4265–4272.
55 G. Li, D. Jiang, H. Wang, X. Lan, H. Zhong and Y. Jiang, *J. Power Sources*, 2014, **265**, 325–334.
56 J. Gopalakrishnan and K. K. Rangan, *Chem. Mater.*, 1992, **4**, 745–747.
57 Q. Zhou, L. Wang, W. Li, S. Zeng, K. Zhao, Y. Yang, Q. Wu, M. Liu, Q.-a. Huang, J. Zhang and X. Sun, *ACS Appl. Mater. Interfaces*, 2021, **13**, 25036–25043.
58 D. Yan, X. Li, S. Xiao, Z. Li, J. Jiang, R. Wu and J. S. Chen, *ChemElectroChem*, 2021, **8**, 3538–3543.
59 S. Sun, Y. Chen, J. Cheng, Z. Tian, C. Wang, G. Wu, C. Liu, Y. Wang and L. Guo, *Chem. Eng. J.*, 2021, **420**, 130453.
60 J. Xu, E. Gu, Z. Zhang, Z. Xu, Y. Xu, Y. Du, X. Zhu and X. Zhou, *J. Colloid Interface Sci.*, 2020, **567**, 84–91.
61 M. Li, Q. Zhang, Z. Zuo, X.-W. Gao, Q. Yao, Z. Wang, W.-B. Luo, H. Zhou and J. Deng, *J. Nanopart. Res.*, 2020, **22**, 1–9.

62 M. Guo, J. Wang, H. Dou, G. Gao, S. Wang, J. Wang, Z. Xiao, G. Wu, X. Yang and Z.-F. Ma, *Nano Energy*, 2019, **56**, 502–511.

63 J. Yang, D. Li, X. Wang, X. Zhang, J. Xu and J. Chen, *Energy Storage Mater.*, 2020, **24**, 694–699.

64 Y. Wang, W. Yang, X. Zhang, W. He, C. Wei, X. Yi, Z. Wang, Q. Cheng and J. Ma, *J. Alloys Compd.*, 2019, **777**, 784–794.

65 B. Zhang, T. Zeng, Y. Liu and J.-f. Zhang, *RSC Adv.*, 2018, **8**, 5523–5531.

66 W. Song, Z. Wu, J. Chen, Q. Lan, Y. Zhu, Y. Yang, C. Pan, H. Hou, M. Jing and X. Ji, *Electrochim. Acta*, 2014, **146**, 142–150.

67 H. Wang, D. Jiang, Y. Zhang, G. Li, X. Lan, H. Zhong, Z. Zhang and Y. Jiang, *Electrochim. Acta*, 2015, **155**, 23–28.

68 Q. Wang, H. Gao, J. Li, G.-B. Liu and H. Jin, *ACS Appl. Mater. Interfaces*, 2021, **13**, 14325–14333.

69 L. Zhao, H. Zhao, Z. Du, N. Chen, X. Chang, Z. Zhang, F. Gao, A. Trenczek-Zajac and K. Świerczek, *Electrochim. Acta*, 2018, **282**, 510–519.

70 Y. Huang, X. Li, J. Wang, L. Miao, C. Li, J. Han and Y. Huang, *Energy Storage Mater.*, 2018, **15**, 108–115.

71 B. Chen, Z. Peng and Z. Yuan, *Ceram. Int.*, 2022, **48**, 33957–33966.

72 C. Liu, C. Qian, H. Dong, Z. Lu, Q. Huang and Y. Chen, *Compos. Commun.*, 2023, **40**, 101610.

73 Y. Chen, X. Liao, P. Wang, J. Chen, X. Zhang, X. Wu, S. C. Smith, D. Lin, X. Tan and Q. Zheng, *J. Colloid Interface Sci.*, 2024, **653**, 1–10.

74 X. Li, Y. Huang, J. Wang, L. Miao, Y. Li, Y. Liu, Y. Qiu, C. Fang, J. Han and Y. Huang, *J. Mater. Chem. A*, 2018, **6**, 1390–1396.

75 T. Tong, Z. Tian, W. Chen, Y. Linghu, D. Li, Z. Tian, Y. Wang, Y. Chen and L. Guo, *Electrochim. Acta*, 2022, **411**, 140073.

76 J. Zhang, X. Zhao, Y. Song, Q. Li, Y. Liu, J. Chen and X. Xing, *Energy Storage Mater.*, 2019, **23**, 25–34.

77 Q. Zheng, X. Ni, L. Lin, H. Yi, X. Han, X. Li, X. Bao and H. Zhang, *J. Mater. Chem. A*, 2018, **6**, 4209–4218.

78 J. Cong, S.-h. Luo, P.-y. Li, X. Yan, L.-x. Qian and S.-x. Yan, *Appl. Surf. Sci.*, 2024, **643**, 158646.

79 J. Cong, S.-h. Luo, P.-y. Li, K. Li, P.-w. Li and S.-x. Yan, *J. Energy Storage*, 2023, **72**, 108808.

80 P. Hu, X. Wang, T. Wang, L. Chen, J. Ma, Q. Kong, S. Shi and G. Cui, *Adv. Sci.*, 2016, **3**, 1600112.

81 Q. Wang, Q. Wang, M. Zhang, B. Han, C. Zhou, Y. Chen and G. Lv, *J. Mol. Model.*, 2019, **25**, 96.

82 J. M. Le Meins, M. P. Crosnier-Lopez, A. Hemon-Ribaud and G. Courbion, *J. Solid State Chem.*, 1999, **148**, 260–277.

83 R. A. Shakoor, D.-H. Seo, H. Kim, Y.-U. Park, J. Kim, S.-W. Kim, H. Gwon, S. Lee and K. Kang, *J. Mater. Chem.*, 2012, **22**, 20535–20541.

84 K. Lin, Q. Liu, Y. Zhou, H. Chen, J. Liu, J.-Z. Zhao and X. Hou, *Chem. Eng. J.*, 2023, **463**, 142464.

85 X. Yi, H. Luo, Y. Zhou, S. Feng, J. Wang, Z. Wang, J. Duan, D. Wang, H. Guo and G. Yan, *Electrochim. Acta*, 2023, **437**, 141491.

86 J. Geng, F. Li, S. Ma, J. Xiao and M. Sui, *Int. J. Electrochem. Sci.*, 2016, **11**, 3815–3823.

87 J. Zhang, Y. Lai, P. Li, Y. Wang, F. Zhong, X. Feng, W. Chen, J. Liu, X. Ai, H. Yang and Y. Cao, *Green Energy Environ.*, 2022, **7**, 1253–1262.

88 H. Yi, M. Ling, W. Xu, X. Li, Q. Zheng and H. Zhang, *Nano Energy*, 2018, **47**, 340–352.

89 L. Li, Y. Xu, R. Chang, C. Wang, S. He and X. Ding, *Energy Storage Mater.*, 2021, **37**, 325–335.

90 J. Nongkynrih, A. Sengupta, B. Modak, S. Mitra, A. K. Tyagi and D. P. Dutta, *Electrochim. Acta*, 2022, **415**, 140256.

91 S.-H. Zhuang, C.-C. Yang, M. Zheng, S. Rengapillai, S. Marimuthu, Y.-S. Chiang, B. K. Chang, C.-H. Huang and W.-R. Liu, *Surf. Coat. Technol.*, 2022, **434**, 128184.

92 S. C. C. van der Lubbe, Z. Wang, D. K. J. Lee and P. Canepa, *Chem. Mater.*, 2023, **35**, 5116–5126.

93 F. L. Chen, V. M. Kovrugin, R. David, O. Mentré, F. Fauth, J.-N. Chotard and C. Masquelier, *Small Methods*, 2019, **3**, 1800218.

94 S. Ghosh, N. Barman, M. Mazumder, S. K. Pati, G. Rousse and P. Senguttuvan, *Adv. Energy Mater.*, 2020, **10**, 1902918.

95 H. Gao, I. D. Seymour, S. Xin, L. Xue, G. Henkelman and J. B. Goodenough, *J. Am. Chem. Soc.*, 2018, **140**, 18192–18199.

96 H. Gao, Y. Li, K. Park and J. B. Goodenough, *Chem. Mater.*, 2016, **28**, 6553–6559.

97 J. Wang, Y. Wang, D.-H. Seo, T. Shi, S. Chen, Y. Tian, H. Kim and G. Ceder, *Adv. Energy Mater.*, 2020, **10**, 1903968.

98 J. Li, X. Zhao, P. He, Y. Liu, J. Jin, Q. Shen, Y. Wang, S. Li, X. Qu, Y. Liu and L. Jiao, *Small*, 2022, **18**, 2202879.

99 F. Chen, V. M. Kovrugin, R. David, O. Mentré, F. Fauth, J.-N. Chotard and C. Masquelier, *Small Methods*, 2019, **3**, 1800218.

100 H. Li, M. Xu, C. Gao, W. Zhang, Z. Zhang, Y. Lai and L. Jiao, *Energy Storage Mater.*, 2020, **26**, 325–333.

101 Y. Liu, X. Rong, R. Bai, R. Xiao, C. Xu, C. Zhang, J. Xu, W. Yin, Q. Zhang, X. Liang, Y. Lu, J. Zhao, L. Chen and Y.-S. Hu, *Nat. Energy*, 2023, **8**, 1088–1096.

102 T. Zhu, W. Liu, X. Liao, M. Wang, H. Fan, Z. Wei, C. Cai, L. Yang, M. Li, D. Wang, P. Hu and X. Wang, *Adv. Fiber Mater.*, 2024, **6**, 561–569.

103 F. d'Yvoire, M. Pintard-Scrépel, E. Bretey and M. de la Rochère, *Solid State Ionics*, 1983, **9–10**, 851–857.

104 I. L. Matts, S. Dacek, T. K. Pietrzak, R. Malik and G. Ceder, *Chem. Mater.*, 2015, **27**, 6008–6015.

105 M. Mamoor, R. Lian, D. Wang, Y. Dou, Y. Wang, Y. Yu, C. Wang, G. Chen and Y. Wei, *Electrochim. Acta*, 2021, **379**, 138157.

106 G. Taveri, A. Güneren, M. Barlog, M. Hnatko, I. Zhukova, Z. Netriova, E. Šimon, M. Mičušik, M. Mikolášek and H. Kaňková, *J. Power Sources*, 2024, **592**, 233917.

107 P. Feng, W. Wang, J. Hou, K. Wang, S. Cheng and K. Jiang, *Chem. Eng. J.*, 2018, **353**, 25–33.

108 D. Guo, F. Wang, M. Yang, G. Hu, G. Liu, N. Wu, A. Qin and X. Liu, *Electrochim. Acta*, 2022, **424**, 140695.

109 M. Ling, Q. Jiang, T. Li, C. Wang, Z. Lv, H. Zhang, Q. Zheng and X. Li, *Adv. Energy Mater.*, 2021, **11**, 2100627.

110 M. Mamoor, R. Lian, D. Wang, X. Meng, G. Chen and Y. Wei, *Phys. Chem. Chem. Phys.*, 2019, **21**, 14612–14619.

111 Y. Zuo, J. Yue, Z. Ma and Z. Zuo, *J. Phys. Chem. Solids*, 2022, **160**, 110354.

112 Y. Lu, S. Zhang, Y. Li, L. Xue, G. Xu and X. Zhang, *J. Power Sources*, 2014, **247**, 770–777.

113 D. A. Aksyonov, S. S. Fedotov, K. J. Stevenson and A. Zhugayevych, *Comput. Mater. Sci.*, 2018, **154**, 449–458.

114 H. Li, H. Tang, C. Ma, Y. Bai, J. Alvarado, B. Radhakrishnan, S. P. Ong, F. Wu, Y. S. Meng and C. Wu, *Chem. Mater.*, 2018, **30**, 2498–2505.

115 V. Soundharrajan, M. H. Alfaruqi, S. Lee, B. Sambandam, S. Kim, S. Kim, V. Mathew, P. Duong Tung, J.-Y. Hwang, Y.-K. Sun and J. Kim, *J. Mater. Chem. A*, 2020, **8**, 12055–12068.

116 T. Wu, J. Sun, Z. Q. Jeremy Yap, M. Ke, C. Y. H. Lim and L. Lu, *Mater. Des.*, 2020, **186**, 108287.

117 T. Zhu, W. Liu, X. Liao, M. Wang, H. Fan, Z. Wei, C. Cai, L. Yang, M. Li, D. Wang, P. Hu and X. Wang, *Adv. Fiber Mater.*, 2024, **6**, 561–569.

118 Q. Deng, Q. Cheng, X. Liu, C. Chen, Q. Huang, J. Li, W. Zhong, Y. Li, J. Hu, H. Wang, L. Wu and C. Yang, *Chem. Eng. J.*, 2022, **430**, 132710.

119 P. Hu, X. Wang, J. Ma, Z. Zhang, J. He, X. Wang, S. Shi, G. Cui and L. Chen, *Nano Energy*, 2016, **26**, 382–391.

120 P. Senguttuvan, G. Rousse, M. E. Arroyo y de Dompablo, H. Vezin, J. M. Tarascon and M. R. Palacin, *J. Am. Chem. Soc.*, 2013, **135**, 3897–3903.

121 Q. Wang, S. He, H. Chen, Z. Peng, Z. Xu, Z. Zeng, C. Wang, P. Xue, L. Ni, X. Li, J. Han and Q. Wang, *Green Chem.*, 2024, **26**, 2114–2123.

122 B. He, K. Yin, W. Gong, Y. Xiong, Q. Zhang, J. Yang, Z. Wang, Z. Wang, M. Chen, P. Man, P. Coquet, Y. Yao, L. Sun and L. Wei, *Nano Energy*, 2021, **82**, 105764.

123 J. Li, Z. Li, S. Tang, T. Wang, K. Wang, L. Pan and C. Wang, *J. Colloid Interface Sci.*, 2023, **629**, 121–132.

124 X. Wang, P. Hu, L. Chen, Y. Yao, Q. Kong, G. Cui, S. Shi, L. Chen and X. Wang, *J. Mater. Chem. A*, 2017, **5**, 3839–3847.

125 P. Feng, W. Wang, J. Hou, Q. Jin, K. Wang and K. Jiang, *J. Power Sources*, 2020, **463**, 228194.

126 X. Ou, X. Liang, C. Yang, H. Dai, F. Zheng, P. Wu, Q. Pan, X. Xiong and M. Liu, *Energy Storage Mater.*, 2018, **12**, 153–160.

127 Y. Zou, A. Tang, C. Shang, P. Hu, Z. Zhang and Z. Huang, *Mater. Lett.*, 2022, **319**, 132216.

128 D. Park, K. Kim, G. H. Chun, B. C. Wood, J. H. Shim, S. Yu and D. Park, *J. Mater. Chem. A*, 2021, **9**, 23037–23045.

129 K. Singh, A. Chakraborty, R. Thirupathi and S. Omar, *Ionics*, 2022, **28**, 5289–5319.

130 Y. Wang, S. Song, C. Xu, N. Hu, J. Molenda and L. Lu, *Nano Mater. Sci.*, 2019, **1**, 91–100.

131 C. Wang, J. Liang, Y. Zhao, M. Zheng, X. Li, X. Sun and C. Wang, *Energy Environ. Sci.*, 2021, **14**, 2577–2619.

132 Y. Lu, L. Li, Q. Zhang, Z. Niu and J. Chen, *Joule*, 2018, **2**, 1747–1770.

133 A. Banerjee, K. H. Park, J. W. Heo, Y. J. Nam, C. K. Moon, S. M. Oh, S.-T. Hong and Y. S. Jung, *Angew. Chem.*, 2016, **128**, 9786–9790.

134 T. Fuchs, S. P. Culver, P. Till and W. G. Zeier, *ACS Energy Lett.*, 2019, **5**, 146–151.

135 Z. Zhang, E. Ramos, F. Lalère, A. Assoud, K. Kaup, P. Hartman, L. F. Nazar and Z. Zhang, *Energy Environ. Sci.*, 2018, **11**, 87–93.

136 C. Fu, Y. Li, W. Xu, X. Feng, W. Gu, J. Liu, W. Deng, W. Wang, A. M. M. Abeykoon, L. Su, L. Zhu, X. Wu and H. Xiang, *Nat. Commun.*, 2024, **15**, 4315.

137 L. Hu, H. Li, F. Chen, Y. Liu, J. Wang and C. Ma, *J. Energy Chem.*, 2024, **95**, 1–8.

138 X. Feng, H. Fang, P. Liu, N. Wu, E. C. Self, L. Yin, P. Wang, X. Li, P. Jena, J. Nanda and D. Mitlin, *Angew. Chem., Int. Ed.*, 2021, **60**, 26158–26166.

139 A. Nasu, T. Inaoka, F. Tsuji, K. Motohashi, A. Sakuda, M. Tatsumisago and A. Hayashi, *ACS Appl. Mater. Interfaces*, 2022, **14**, 24480–24485.

140 S. Abouricha, A. Ihechmyen, H. Aziam, H. A. Said, A. Ouarga, N. Oueldna, N. Sabi, H. Noukrati, M. Lahcini, I. Saadoune and H. Ben youcef, *J. Energy Storage*, 2024, **91**, 111967.

141 X.-Y. Niu, X.-Y. Dou, C.-Y. Fu, Y.-C. Xu and X.-Y. Feng, *RSC Adv.*, 2024, **14**, 14716–14721.

142 Z. L. Dong, Y. Yuan, V. Martins, E. Jin, Y. Gan, X. Lin, Y. Gao, X. Hao, Y. Guan, J. Fu, X. Pang, Y. Huang, Q. H. Tu, T.-K. Sham and Y. Zhao, *Nano Energy*, 2024, **128**, 109871.

143 A. J. K. Tieu, E. Mahayoni, Y. Li, Z. Deng, F. Fauth, J.-N. Chotard, V. Seznec, S. Adams, C. Masquelier, P. Canepa and A. J. K. Tieu, *J. Mater. Chem. A*, 2023, **11**, 23233–23242.

144 K. B. Hueso, V. Palomares, M. Armand and T. Rojo, *Nano Res.*, 2017, **10**, 4082–4114.

145 S.-F. Ho and H.-Y. Tuan, *Chem. Eng. J.*, 2023, **452**, 139199.

146 S. J. Hussain, J. Liu, P.-H. Du, M. A. Nazir, Q. Sun and P. Jena, *ACS Appl. Mater. Interfaces*, 2024, **16**, 14364–14370.

147 K. M. Bui, V. A. Dinh, S. Okada, T. Ohno and K. M. Bui, *Phys. Chem. Chem. Phys.*, 2016, **18**, 27226–27231.

148 H. Park, K. Jung, M. Nezafati, C.-S. Kim and B. Kang, *ACS Appl. Mater. Interfaces*, 2016, **8**, 27814–27824.

149 H. Wang, G. Zhao, S. Wang, D. Liu, Z. Mei, Q. An, J. Jiang, H. Guo and H. Wang, *Nanoscale*, 2022, **14**, 823–832.

150 J. Wang, T. He, X. Yang, Z. Cai, Y. Wang, V. Lacivita, H. Kim, B. Ouyang and G. Ceder, *Nat. Commun.*, 2023, **14**, 5210.

151 M. L. Adam, O. A. Moses, J. P. Mailoa, C.-Y. Hsieh, X.-F. Yu, H. Li and H. Zhao, *Energy Storage Mater.*, 2024, **65**, 103090.

152 T. Yu, C. Wang, H. Yang and F. Li, *J. Energy Chem.*, 2024, **90**, 191–204.